# The large-scale context for oceanic subduction in the Northeast Atlantic

R.A. Weller[a],*, P.W. Furey[a], M.A. Spall[a], R.E. Davis[b]

[a] *Woods Hole Oceanographic Institution, Woods Hole, MA 02543, USA*
[b] *Scripps Institution of Oceanography, La Jolla, CA 92037, USA*

## Abstract

The large-scale context for oceanic subduction is examined in the region bounded by $10°N$ and $40°N$ and $10°W$ and $40°W$ using data collected from June 1991 to June 1993. In contrast to climatology, it was found that over the entire region the ocean gained heat, ranging from $10–30 \, W \, m^{-2}$ to the north to $40–50 \, W \, m^{-2}$ to the south. Steady tradewinds dominated the southeastern half of the region. To the northwest of the axis of these tradewinds was a broad region of downward Ekman pumping with a 2-yr mean of about $50 \, m \, yr^{-1}$. Wind-driven surface currents and a seasonal cycle in mixed layer temperature and depth were found that reflected the influence of local forcing. The interior circulation was consistent with the clockwise circulation of the eastern end of the subtropical gyre, though eddy variability dominated the northern part of the region. Due to Ekman convergence the winter mixed layer in the central and southwestern parts of the region was as deep as to the north; however, it was also warm. This deep, warm mixed layer in the center of the region aided the subduction of water from the northeast by providing a protective cap; isopycnals that outcropped to the north passed well below the base of this mixed layer.
© 2004 Elsevier Ltd. All rights reserved.

## 1. Introduction

Oceanic subduction refers to the processes by which mixed layer waters are incorporated into the main thermocline (Stommel, 1979; Luyten et al., 1983). Ekman pumping contributes to water being isolated from the mixed layer as does lateral induction (Marshall et al., 1993). The seasonal cycle of the upper ocean plays, in particular, an important role in subduction (Woods, 1985; Qiu

and Huang, 1995; Paillet and Ahran, 1996) with spring restratification capping over the deep mixed layer formed during the previous winter, as evidenced by the match between the T/S properties of the thermocline in the Northeast Atlantic (Montgomery, 1938) and those of the late winter mixed layer. It is probable that the loss of water from the mixed layer is also spatially modulated. Fronts, for example, are thought to be a site of active subduction (Rudnick and Luyten, 1996; Rudnick, 1996; Pollard and Regier, 1992).

However, a perspective on subduction that dates from Montgomery (1938) and Iselin (1939) is that large-scale spatial gradients and the seasonal cycle

*Corresponding author. Tel.: +1-508-289-2508; fax: +1-508-457-2163.

*E-mail address:* rweller@whoi.edu (R.A. Weller).

in atmospheric forcing are central to the subduction process in the eastern subtropical Atlantic, a region referred to here as the Northeast Atlantic. Over that region, one supposes that the large-scale surface forcing is characterized in the winter by episodic strong winds and greater heat loss to the north. Further, one supposes that mixed layer water formed in the winter enters the upper thermocline and is carried by the clockwise geostrophic flow of the mid-latitude gyre to the southwest where in subsequent winters the mixed layers are shallower, ensuring that the water is not entrained again into the mixed layer. Certainly, Jenkins (1998) tritium–helium dating of water on isopycnal surfaces in the upper thermocline in the Northeast Atlantic, which shows smooth age gradients along isopycnals that slope down towards the southwest, is consistent with this notion.

It is from this perspective that we investigated subduction in the eastern half of the subtropical gyre in the North Atlantic, which we shall call the Northeast Atlantic. Observations were collected during the cooperative Subduction Experiment from June 1991 to June 1993. The Northeast Atlantic was chosen as the location for the fieldwork because the anticyclonic curl of the wind stress associated with the Azores-Bermuda high causes Ekman convergence and pumping and because it was anticipated that strong annual variability and large-scale latitudinal gradients would be found in the surface forcing. These latitudinal gradients would in turn lead to shoaling of the winter mixed layer to the south, which would prevent re-entrainment.

Prior to the experiment, our understanding of the surface forcing in the Northeast Atlantic was limited, and one emphasis in our effort was on the collection and analysis of surface forcing data in the region roughly bounded by 10°N and 40°N and 10°W and 40°W. In situ surface meteorology obtained from the widely spaced array of surface moorings was supplemented with the surface analyses from the European Centre for Medium Range Weather Forecasts (ECMWF) numerical weather prediction model. Another emphasis was on the collection of the time series of ocean currents and temperature, mainly above the seasonal thermocline, needed to investigate the

variability of the upper ocean, including its response to local forcing, the spatial and temporal variability of the depth of the mixed layer, and the velocities in and below the mixed layer. Additional temperature information came from XBTs and Lagrangian profiling floats, which also provided Lagrangian velocities.

Our analysis is based on both observations and modeling. In this paper, we discuss the observational component of the work, drawing principally on data from the widely spaced ($\sim 1300$ km $\times$ 1300 km) array of surface moorings designed to directly observe the large-scale gradients in the net heat and freshwater fluxes and wind stress while simultaneously monitoring the response of the upper ocean. A companion paper (Spall et al., 2000) complements the discussion, incorporating results from a three-dimensional ocean model. Using the field data, we seek here to answer the following questions:

- Is there a latitudinal gradient in surface forcing?
- Do large-scale gradients in buoyancy forcing and wind stress lead to a shoaling of the mixed layer to the south or southwest?
- Is there a region of Ekman convergence?
- How like the clockwise Sverdup circulation described by Huang (1989) and others is the thermocline flow in the Northeast Atlantic?
- How like Stommel's (1979) Ekman demon are the seasonal meridional progression in the thermal structure and the progression of the subducted water into the upper thermocline?
- Is there evidence of subduction in part or all of the region?

An overview of the data is provided in Section 2. The atmospheric forcing of the region is summarized in Section 3, drawing from both climatologies and the data from 1991 to 1993. The thermal variability of the upper ocean is described and compared with climatology with an emphasis on the seasonal cycle and large-scale spatial gradients in Section 4. The observed velocity variability is presented in Section 5. The extent to which the observed variability can be attributed to local forcing is identified in Section 6. Section 7 discusses the findings from the perspective of subduction.

## 2. Data from the Northeast Atlantic

Upper ocean temperature variability was observed in the Northeast Atlantic from the array of surface moorings, with XBTs, and with profiling floats. The siting of the array and the instrumentation deployed on the moorings are described in Section 2.1. The meteorological data from the buoys were used to compute time series of the air–sea fluxes, and the observed fluxes were used in the development of gridded surface forcing fields for the Northeast Atlantic ($1°$ grid, hourly time resolution, $10–40°$N, $10–40°$W) (Section 2.2). The oceanographic instrumentation on the moorings are described in Section 2.3. The XBT data and the use of this data in conjunction with the mooring data to determine mixed layer depths are described in Section 2.4. The use of the Lagrangian profilers is described in Section 2.5.

### 2.1. The subduction moored array

The locations of the five surface moorings deployed during the cooperative Subduction Experiment from June 1991 to June 1993 (Table 1) are shown in Fig. 1 relative to climatological mean surface forcing fields, the general ocean circulation, and the annual migration of the surface isopycnals. In the tropical Atlantic the density outcrops move north and south by roughly $20°$ of latitude over an annual cycle (Fig. 1b). In sizing the array, a latitudinal range of $15–20°$ was chosen to match this seasonal migration and to span the eastern end of the Azores-Bermuda high pressure cell (Fig. 1c) and its broad pattern of convergent, wind-driven surface flow. The array was positioned to straddle the zero line in the climatological net heat flux (Fig. 1d), with the intent of

sampling under both net heating to the south and net cooling to the north. To avoid placing any of the moorings in frontal regions, the array elements were kept within the subtropical gyre, south of the Azores front and north of the subtropical front (Fig. 1a). The resulting array had four corner sites forming a $1300\,km \times 1300\,km$ square with a fifth site in the center. In this paper, the moorings, identified by the capital letter designations given in Table 1, will be used as geographical reference points while discussing the Northeast Atlantic.

This array of five surface moorings was deployed for 2 yr as a collaborative effort between the Woods Hole Oceanographic Institution (WHOI) and Scripps Institution of Oceanography (SIO). The 2 yr deployment was accomplished with three consecutive settings, each 8 months long, with recovery and redeployment in both February and October 1992. Maintaining the moorings proved to be a technological challenge, and mooring failures resulted in some gaps (Brink et al., 1995). There are no gaps at C and NE other than those associated with the mooring turnarounds. Data for 62%, 83%, and 62% of the 2 yr were recovered at SW, SE, and NW, respectively, with the largest gaps at the end of the first deployment for each.

### 2.2. Surface meteorology and air–sea fluxes

Surface meteorological data were collected on the five surface moorings with Vector Averaging Wind Recorders (VAWR; Weller et al., 1990) and Improved METeorogical Recorders (IMET; Hosom et al., 1995). Both measured barometric pressure, wind speed and direction, air temperature, sea temperature, relative humidity, incoming shortwave radiation, and incoming longwave radiation. The IMET system also measured precipitation. Calibrations, intercomparisons, and discussion of the accuracy of the meteorological data and derived fluxes are given in Moyer and Weller (1997).

Synoptic weather charts for the North Atlantic and the gridded analysis and forecast fields from the European Centre for Medium Range Weather Forecasts (ECMWF) and the National Centers for Environmental Prediction (NCEP) were also obtained for years prior to 1991 as well as for

Table 1
Subduction mooring locations

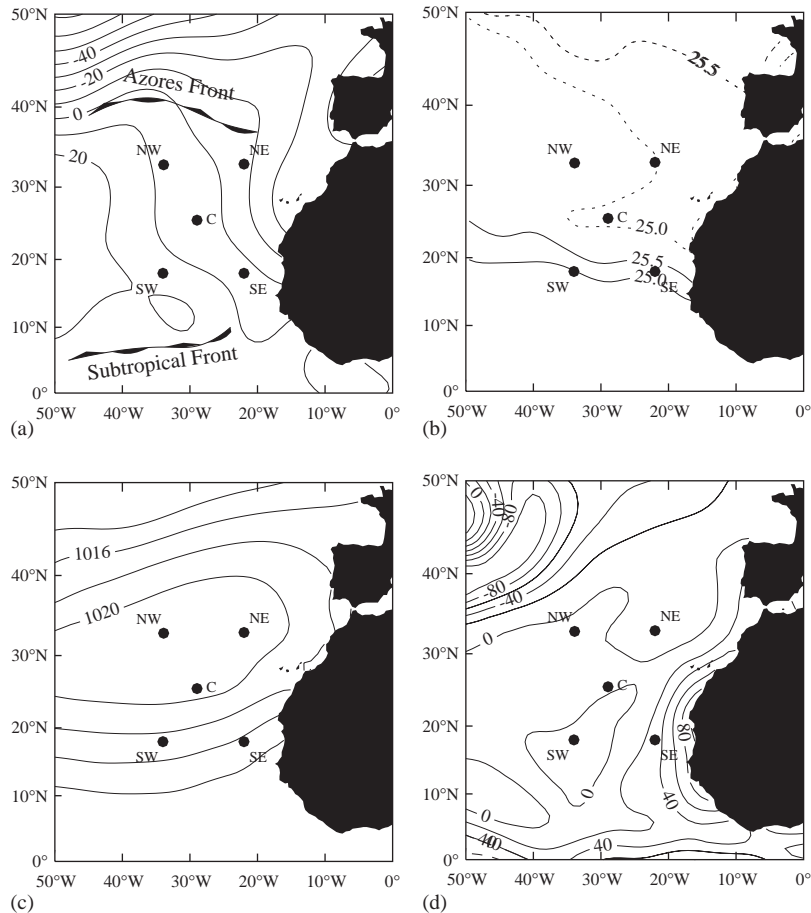| Mooring | Latitude | Longitude |
|---------|----------|-----------|
| NE | $33°$N | $22°$W |
| NW | $33°$N | $34°$W |
| C | $25.5°$N | $29°$W |
| SE | $18°$N | $22°$W |
| SW | $18°$N | $34°$W |

Fig. 1. Maps of the northeast Atlantic, showing (a) the location of the 5 surface moorings along with the locations of the Azores front after Pingree and Sinha (1999) and the subtropical front after Tapley et al. (1994), along with the dynamic topography computed from WOA-94 (1994), (b) the northernmost (dashed lines) and southernmost (solid lines) surface locations of the 25.0 and 25.5 kg m$^{-3}$ surface isopycnals based on the temperature and salinity fields from Levitus and Boyer (1994) and Levitus et al. (1994), (c) the annual mean surface pressure field (da Silva et al., 1994), and (d) the annual mean net air–sea heat flux (da Silva et al., 1994), with positive indicating ocean heating.

the period of the experiment. The surface meteorology and air–sea fluxes from the moorings were compared with climatologies and with these numerical weather prediction model fields (Moyer and Weller, 1997). Based on the good agreement between the buoy data and ECMWF surface fields, gaps when the buoys were not on station were filled by the meteorological data from the ECMWF analyses. As the ECMWF analyses are only available at 0,6,12, and 18 UTC, the ECMWF data were, with the exception of incoming shortwave and longwave radiation, linearly interpolated to the 15 min sampling rate of the moored data. Relative humidity was calculated from ECMWF air temperature, dew point temperature, and barometric pressure using a variation of Teten's formula (Bolton, 1980). The gaps in incoming shortwave data were filled using cloud cover data from ECMWF to modify computed 15 min time series of clear sky incoming shortwave radiation; Appendix A provides more detail on this procedure.

Air–sea fluxes were computed using the bulk formulae of Fairall et al. (1996b). Cool skin and

warm layer corrections as incorporated into the Fairall et al. (1996a) algorithm were used to determine sea surface temperature from the shallowest observed temperature, which came from a depth of 1 m. Moyer and Weller (1997) examined the accuracy of the resulting fluxes; their conclusions for monthly and longer-term average values are summarized in Appendix B, Table 11. Air–sea flux fields were developed using the ECMWF basic observables (except for precipitation, which came from NCEP), the COARE bulk flux formulae, the mooring data, and interpolation to produce hourly time series running from June 1, 1991 to June 26, 1993 on a $1°$ grid between 10–40°N and 10°N to 40°W. The preparation of the gridded forcing data is described in Appendix B. Comparison of the net heat flux provided by ECMWF with the buoy net heat flux and the mean heat flux from the derived gridded flux fields is also provided in that appendix (Table 12). The gridded fields allowed us to examine the spatial variability of the atmospheric forcing and also to force the ocean model in the studies described in Spall et al. (2000).

## 2.3. Oceanic velocity and temperature data from the moored array

The five moorings carried current meters and temperature recorders. NE, C, SW, and SE were equipped with Vector Measuring Current Meters (VMCMs) (Weller and Davis, 1980) which measured horizontal velocity and temperature, while NW was equipped with an upward looking Acoustic Doppler Current Profiler (ADCP) located at 110 m. Temperature was also measured using Brancker Temperature Recorders attached to the moorings. Table 2 summarizes the measurement depths. The gaps of between 1 and 5 days between the successive settings of the moorings were filled with linear interpolation. Several instruments failed to record complete records, but the majority of the gaps in the mooring data were associated with the periods of time that the moorings were not on station. Basic recording rates ranged from 7.5 to 30 min, with most instruments recording every 15 min. The VMCM speeds are accurate to approximately 2% above

Table 2
Sampling depths for velocity ($V$) and temperature ($T$) on the Subduction surface moorings

| Depth (m) | NE | NW | C | SW | SE |
|---|---|---|---|---|---|
| 1 | T | T | T | T | T |
| 10 | T, V | T, V* | T, V | T, V | T, V |
| 30 | T, V | T, V* | T, V | T, V | T, V |
| 50 | T, V | T, V* | T, V | T, V | T, V |
| 60 | T | T, V* | T | T | T |
| 70 | T, V | T, V* | T, V | T, V | T |
| 80 | T | T, V* | T | T | T |
| 90 | T, V | T, V* | T, V | T, V | T |
| 100 | T | T, V* | T | T | T |
| 110 | T, V | T, V | T, V | T, V | T |
| 130 | T | T | T | T | T |
| 150 | T, V | T, V | T, V | T, V | T |
| 200 | T, V | T, V | T, V | T, V | T |
| 300 | T | T | T | T | T |
| 400 | T | T | T | T | T |
| 580 | T | T | T | T | T |
| 750 | T | T | T, V | T | T |
| 1500 | T | T | T, V | T | T |
| 3500 | | | T, V | | |

$V*$ denotes velocities sampled with an upward–looking ADCP. Other velocities, $V$, were sampled with VMCMs.

threshold speeds, and the VMCM flux gate compass has an uncertainty of 2–4°. The temperature time series, after calibration of the VMCMs and temperature recorders, are accurate to approximately 0.01°C.

## 2.4. XBT data and mixed layer depth histories at the mooring sites

During the four mooring cruises 975 underway temperature profiles were obtained with T- 7 XBTs (750 m depth capability). In addition, the ship of opportunity XBTs made from June 1991 to July 1993 from between 10°N and 40°N and between 15°W and 40°W were obtained. All profiles from within 5° of each mooring site were retrieved to fill gaps in the moored temperature records, and mixed layer depth time series were created using the criterion that the mixed layer depth was the depth at which temperature was 0.5°C cooler than the shallowest temperature. At C the rms difference of individual mixed layer depths extracted from the XBTs within 5° of the mooring and

coincident mixed layer depths determined using data from the mooring was 16 m. The choice of 0.5°C as a criterion for mixed layer depth was influenced by our desire to compare mixed layer depths with those from climatologies and to not track transient diurnal mixed layer; use of 0.25°C or of 1.0°C did not yield significantly different results.

## 2.5. Lagrangian profiler deployments

Ten profiling, Lagrangian floats (Autonomous Lagrangian Circulation Explorer or ALACE, Davis et al., 1992) were deployed in the Subduction region along the track between C and NE in February 1992. These floats were ballasted to be neutrally buoyant at a depth of about 400 m and collected temperature profiles to the surface with a vertical resolution of 10 m every 10 days. At the surface after each ascent they telemeter their data via satellite; the satellite also provides the positions of the floats at the beginning and end of each dive. The floats each provided between 50 and 100 profiles. Additional floats were deployed by Price (1996) that profiled up and down between chosen isotherms; these were called bobbers. A total of 39.3 float-years of data from 17 Bobber SOFAR floats and 12 ALACE floats was analyzed. The ALACE floats provided 662 displacements of 10 days each. The Bobbers reported daily positions which were combined to make the equivalent of 785 10-day displacements.

## 3. Surface forcing in the Northeast Atlantic

The surface meteorology, the wind stress, the heat fluxes, and the freshwater flux are described in turn.

### 3.1. Surface meteorology

The climatological surface forcing in the Northeast Atlantic developed by da Silva et al. (1994) and Isemer and Hasse (1985) is dominated by an annual cycle in surface heating with oceanic loss to the north, gain to the south, and a mean of close to zero near the moored array (Fig. 1d) and by the Bermuda/Azores High (Fig. 1c). Much of the

spatial and temporal variability during the year is associated with the annual cycles in the solar insolation and in the strength and position of this subtropical high-pressure system. In the winter the high is typically weak, zonally elongated, and meanders between the latitudes of N and C. In the summer, it is stronger, more nearly circular and usually located poleward of the northern moorings. Thus, typically, the southern mooring sites experience fair weather with persistent Northeast Trades. Lengthy periods of steady winds are interrupted only by an occasional synoptic weather event. At the northern mooring sites, and to a lesser extent at the central mooring, there is historically more seasonal variability with westerly winds more frequent during the winter and spring. This is associated with the passage of extratropical cyclones through and to the north of the northern part of the region. During the spring, summer, and fall, it is typical for the Northeasterly Trades to dominate the northern sites as well as C and the southern sites.

Weather charts from 1991 to 1993 showed that the surface meteorological and flux variability in the Northeast Atlantic occurred, with the exception of infrequent synoptic events, on scales resolved by the moored array. The 2-yr mean gridded fields of surface meteorology differed from the climatology shown in Fig. 1 as the Bermuda/Azores High was several millibars stronger and its zonal axis situated slightly north of its climatological winter position (Moyer and Weller, 1997). This reduced the frequency of westerly winds across the northern and central portion of the array, and led to the anomalous easterly winds evident in the region in the climatological anomaly maps of Young-Molling et al. (1995) during the winter of 1991–1992, the spring of 1992, and the winter of 1992–1993. Still, the Northeast trades during 1991–1993 dominated the surface winds in the southeastern half of the array, at and below the line formed by SW, C, and NE.

The trades, characterized by steadiness in speed and direction, were strongest near SE (Fig. 2), and their strength diminished moving toward the northwest. In the northwestern half, directional variability was greater. Peaks in wind speed and changes in wind direction associated with synoptic
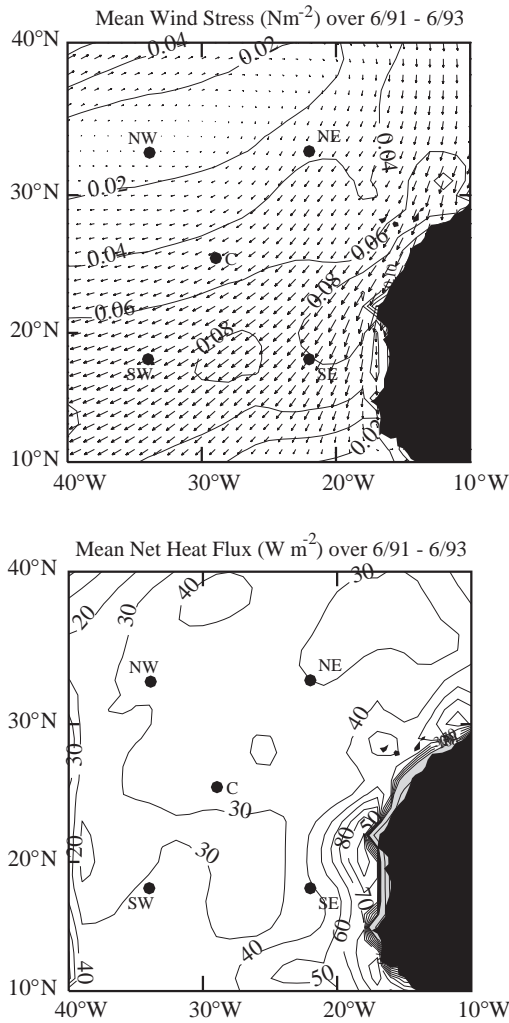
Fig. 2. The 2-yr mean fields of the wind stress (upper, in N m$^{-2}$) and net air–sea heat flux (lower, in W m$^{-2}$) developed from the moored time series and numerical weather prediction model fields of surface meteorology as described in Appendix B.

events at NW are evident in time series from that site (Fig. 3). During the late summer of 1991 through the winter of 1991–1992 the trades in the southeastern region were less well-developed than during the rest of the 2 yr.

### 3.2. Wind stress

In general, due to differences in directional variability, monthly and longer-term vector averages of the wind and wind stress at the buoys decreased in magnitude from southeast to northwest across the array as seen in Fig. 2, while winds scalar averaged at various time scales varied less across the array (Table 3). For these tables the gap-filled buoy time series have been used and summer is the average of June, July, and August, fall is the average of September, October, and November, winter is the average of December, January and February, and spring is the average of March, April, and May.

The gridded wind field was used to examine wind stress curl and Ekman pumping in the Northeast Atlantic during 1991 to 1993. Throughout the annual cycle, the winds drove upwelling along the coast of Africa, east of and near the Cape Verde islands. In the summer that upwelling region extended westward, occupying the area south of SW and SE with a maximum upwelling velocity of 60 m yr$^{-1}$ near 15°N, 27°W. The winds over most of the remainder of the Northeast Atlantic produced downward Ekman pumping; the major exceptions were a $5 \times 5$ region south of NE and east of C in the summer of 1991 with upwelling of less than 20 m yr$^{-1}$ (also seen in the modeling study by Spall et al. (2000) to be a region of upwelling where subduction did not occur) and upwelling in the northern part of the region during winter months that had peak monthly velocities of 40 m yr$^{-1}$ that did not persist for more than 1 month in one location. The region of downward Ekman pumping was largely associated with the spatial structure of the Northeast trades (Fig. 2, upper), with strong downwelling located to the northwest of the axis of the strongest trade winds. The 2-yr mean Ekman pumping field had a $\sim 7°$ wide maximum of downwelling at about 50 m yr$^{-1}$ just south of C, slanting to the west–southwest and bracketing SW; this is similar to the 1941–1972 wclimatological vertical velocities at the base of the mixed layer calculated by Leetmaa and Bunker (1978). During the late summer months the amplitude of this maximum was close to 60 m yr$^{-1}$, shifted to the northwest between C and NW. In the winter and spring months the maximum in downwelling velocity was found further south, typically in or adjacent to the region enclosed by SW, C, and SE, with monthly means of close to 60 m yr$^{-1}$.
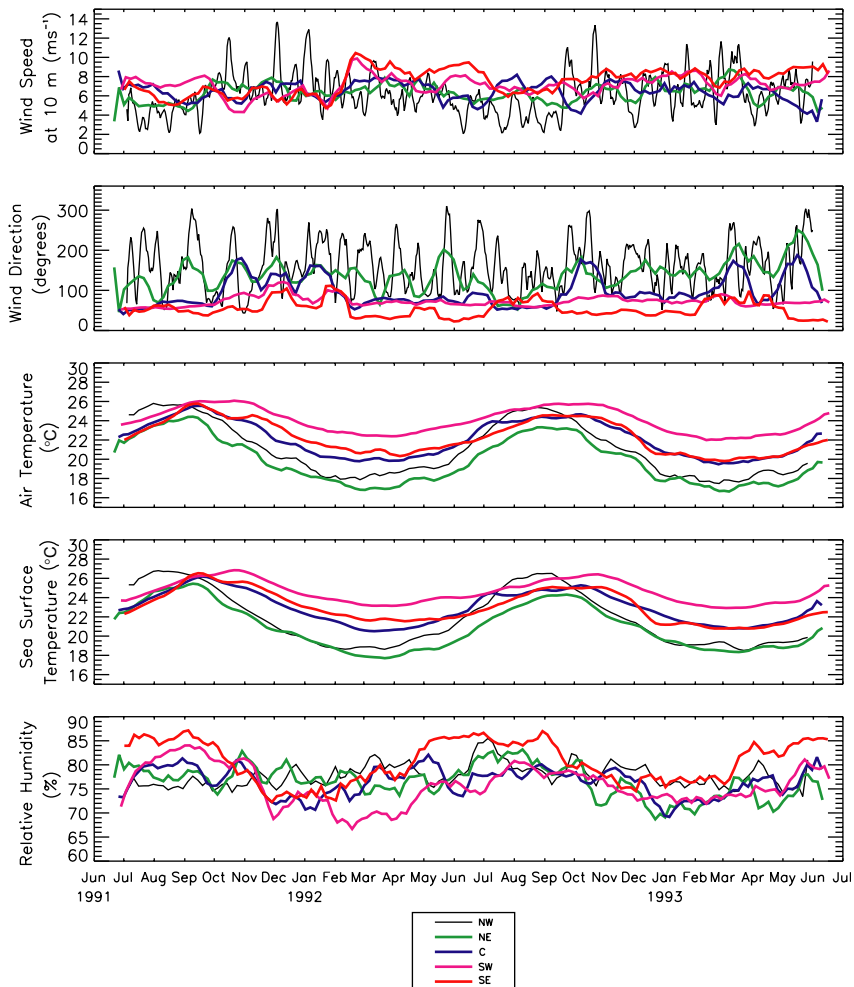
Fig. 3. Forty-eight hour low-passed (running mean) time series (from top to bottom) of the surface wind speed, wind direction, air temperature, sea surface temperature, and relative humidity observed by the surface moorings, with gaps filled using ECMWF.

Table 3
Seasonal and mean, scalar averages of daily wind stress magnitude ($N m^{-2} \times 10^4$)

| Mooring | Summer 91 | Fall 91 | Winter 91–92 | Spring 92 | Summer 92 | Fall 92 | Winter 92–93 | Spring 93 | 91–93 |
|---------|-----------|---------|--------------|-----------|-----------|---------|--------------|-----------|-------|
| NE | 497 | 883 | 797 | 734 | 544 | 861 | 971 | 627 | 739 |
| NW | 391 | 1105 | 965 | 544 | 456 | 910 | 1065 | 706 | 768 |
| C | 630 | 813 | 797 | 674 | 813 | 720 | 745 | 582 | 722 |
| SW | 889 | 545 | 987 | 868 | 713 | 834 | 1042 | 834 | 839 |
| SE | 620 | 625 | 1141 | 1300 | 786 | 1095 | 1130 | 1169 | 837 |

## 3.3. Heat fluxes

Time series of the four components of the heat flux at the five sites (Fig. 4) as well as gridded fields

were computed for 1991–1993 using the buoy data and the gridded surface meteorological data. Seasonal variations in both wind speed and sea–air temperature difference led to an annual cycle in

sensible heat flux that was small in magnitude. Monthly sensible heat losses of less than $5\,W\,m^{-2}$ were typical during the summer, while losses of $10–15\,W\,m^{-2}$ were seen during the winter. The largest sensible heat losses (Fig. 4, Table 4) throughout the year were observed at the northern moorings, and instantaneous losses in excess of $100\,W\,m^{-2}$ were seen there during the winter. Variability in specific humidity reflected that in air temperature, and the air containing the most moisture was found at SW while the air containing the least was at NE. Like the sensible heat losses, latent heat losses across the array were larger in the winter. Monthly oceanic latent heat losses of $75\,W\,m^{-2}$ were common in summer, and losses of $150\,W\,m^{-2}$ were typical in winter. Unlike the sensible heat flux, however, the largest annual latent heat losses (Table 5) were found across the southern portion of the array where substantial air–sea moisture gradients and persistent trade winds were found year round. At the northern moorings, NW in particular, latent heat loss was episodic, with losses in excess of $400\,W\,m^{-2}$ associated with short-lived events.

Intra-annual variations in net shortwave radiation across the array (Fig. 4, Table 6) predominantly reflected seasonal changes in the sun's zenith angle and also the effect of seasonal variations in cloud cover. Monthly net shortwave radiation peaked at $275\,W\,m^{-2}$ in midsummer across the northern moorings and at $250\,W\,m^{-2}$ in late spring across the southern moorings. Minimum monthly net shortwave occurred in December, with 100 and $175\,W\,m^{-2}$ observed at the northern and southern moorings, respectively. In October through March, SE and SW had larger monthly mean shortwave heating than C, which in turn saw more than NE and NW. However, the southern moorings, which received more shortwave energy over the course of the year than the northern moorings, often had low clouds overhead during mid and late summer. This caused the peak in the net shortwave at the southern moorings to occur in the spring rather than in summer. In contrast, clouds were at a minimum during the summer months at the northern moorings. Variations in the net longwave flux across the array (Fig. 3, Table 7) were predominantly a function of

cloud cover and, to a lesser extent, of the near surface atmospheric moisture content. Monthly net longwave losses ranged between 30 and $90\,W\,m^{-2}$ across the array during the 2 yr period with the greatest losses observed in the winter. Summer clouds at the southern moorings led to reduced longwave heat loss there.

All five buoy locations experienced a net oceanic heat gain during the summer months and a net oceanic heat loss during the winter months. The amplitude of the annual range in the monthly net heat flux (Fig. 4) varied from $175\,W\,m^{-2}$ across the southern buoys to $250\,W\,m^{-2}$ across the northern buoys. The latitudinal differences in seasonal averages of shortwave radiation of $30–70\,W\,m^{-2}$ (Table 6), large in the fall and winter, were offset in part by opposing differences in the latent and longwave heat fluxes. As a result, spatial gradients in net heat flux (Table 8) were smaller than those in some of the components. In the two annual averages that could be computed for 1991–1993, the northern buoys and SW experienced net heat gains of $18–20\,W\,m^{-2}$ and SE and C had net gains of $38–44\,W\,m^{-2}$. Both the buoy time series and the gridded fields indicated that the 2-yr mean net heat flux in the Northeast Atlantic was characterized by a broad area of moderate ($\sim 20$ to $40\,W\,m^{-2}$) net annual heat gain by the ocean (Fig. 2, lower) with less heating to the north and the strongest heating at C and SE. This contrasts with the close to zero net heat flux of the da Silva et al. (1994) climatology. A more recent examination of ship-based air–sea fluxes in the region and of the methodology of determination of the fluxes from Volunteer Observing Ship data (Josey, 2001) found good agreement between ship-based fluxes and the moored observations in 1991–1993 and also points to averages over the 1991–1993 period being representative of longer-term means.

There was little change, less than $5\,W\,m^{-2}$ at the moorings, in the annual mean net heat fluxes from the first year to the second year. Year to year variations during a given season were larger. The atmosphere provided $\sim 20\,W\,m^{-2}$ more heat to the ocean across the Northeast Atlantic in both the first summer and the first winter. During the spring and summer of 1992 there was stronger heating of the ocean in the central and northern
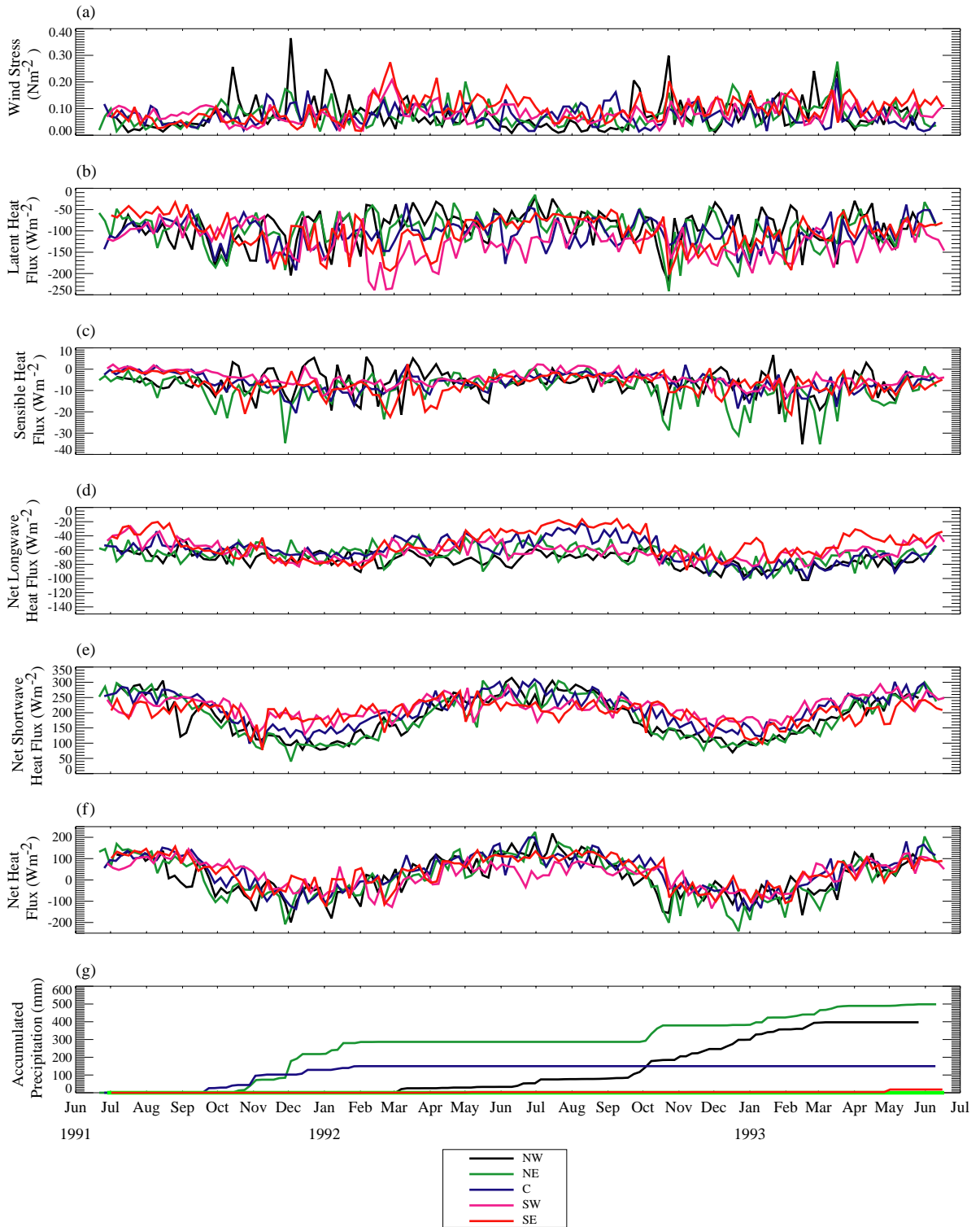
Table 4
Observed seasonal and mean sensible heat flux (W m$^{-2}$)

| Mooring | Summer 91 | Fall 91 | Winter 91–92 | Spring 92 | Summer 92 | Fall 92 | Winter 92–93 | Spring 93 | 91–93 |
|---------|-----------|---------|--------------|-----------|-----------|---------|--------------|-----------|-------|
| NE | –6.9 | –12.4 | –9.0 | –4.8 | –4.6 | –14.2 | –13.2 | –8.9 | –9.2 |
| NW | –6.4 | –5.0 | –6.1 | –5.3 | –5.6 | –7.8 | –9.9 | –5.3 | –6.5 |
| C | –1.6 | –9.3 | –8.9 | –6.0 | –2.6 | –5.9 | –9.7 | –6.4 | –6.3 |
| SW | –0.3 | –4.7 | –6.8 | –4.2 | –1.2 | –5.8 | –7.4 | –4.7 | –4.4 |
| SE | –2.8 | –8.7 | –11.2 | –7.3 | –3.5 | –7.4 | –8.4 | –7.6 | –7.1 |

Table 5
Observed seasonal and mean latent heat flux (W m$^{-2}$)

| Mooring | Summer 91 | Fall 91 | Winter 91–92 | Spring 92 | Summer 92 | Fall 92 | Winter 92–93 | Spring 93 | 91–93 |
|---------|-----------|---------|--------------|-----------|-----------|---------|--------------|-----------|-------|
| NE | –96.1 | –107.2 | –88.1 | –76.1 | –77.2 | –127.2 | –108.6 | –90.9 | –96.4 |
| NW | –105.8 | –113.4 | –84.7 | –70.7 | –80.0 | –98.5 | –94.4 | –82.2 | –91.6 |
| C | –93.8 | –125.9 | –111.2 | –89.9 | –107.5 | –111.0 | –114.6 | –89.6 | –105.4 |
| SW | –96.1 | –114.9 | –160.8 | –135.6 | –109.3 | –139.5 | –144.3 | –119.8 | –127.6 |
| SE | –66.1 | –124.6 | –130.6 | –93.7 | –79.0 | –133.0 | –111.8 | –87.8 | –103.3 |

Table 6
Observed seasonal and mean shortwave radiation (W m$^{-2}$)

| Mooring | Summer 91 | Fall 91 | Winter 91–92 | Spring 92 | Summer 92 | Fall 92 | Winter 92–93 | Spring 93 | 91–93 |
|---------|-----------|---------|--------------|-----------|-----------|---------|--------------|-----------|-------|
| NE | 247.7 | 112.0 | 133.2 | 243.6 | 244.2 | 116.9 | 140.6 | 247.9 | 185.8 |
| NW | 239.4 | 122.2 | 139.5 | 251.1 | 245.9 | 119.9 | 147.4 | 243.0 | 186.2 |
| C | 255.9 | 146.6 | 177.9 | 261.3 | 247.4 | 162.2 | 188.0 | 258.2 | 212.2 |
| SW | 231.1 | 187.9 | 201.7 | 239.3 | 220.2 | 190.8 | 206.7 | 256.3 | 216.8 |
| SE | 216.8 | 178.5 | 203.2 | 232.7 | 211.9 | 178.4 | 168.8 | 209.2 | 199.9 |

Table 7
Observed seasonal and mean net heat longwave (W m$^{-2}$)

| Mooring | Summer 91 | Fall 91 | Winter 91–92 | Spring 92 | Summer 92 | Fall 92 | Winter 92–93 | Spring 93 | 91–93 |
|---------|-----------|---------|--------------|-----------|-----------|---------|--------------|-----------|-------|
| NE | –65.9 | –64.2 | –61.5 | –60.7 | –60.8 | –71.9 | –77.9 | –65.6 | –66.1 |
| NW | –64.6 | –69.6 | –72.7 | –73.0 | –67.3 | –81.7 | –85.3 | –75.3 | –73.6 |
| C | –56.5 | –59.7 | –58.1 | –50.3 | –38.3 | –73.9 | –84.4 | –66.4 | –61.0 |
| SW | –45.5 | –67.2 | –67.7 | –56.2 | –59.2 | –71.1 | –69.2 | –53.9 | –61.3 |
| SE | –41.5 | –68.7 | –66.9 | –42.1 | –24.9 | –64.8 | –58.2 | –42.2 | –51.2 |

parts of the Northeast Atlantic. Weaker heat gain by the ocean in the fall and greater net heat loss in the winter accompanied the stronger northeast trades seen in the second year in the southeastern part of the region. There was stronger cooling of the ocean and more well-defined meridional gradient in that cooling in the second fall and winter, when that cooling was 55 W m$^{-2}$ stronger at NE and NW than at SE and SW.

Fig. 4. Forty-eight hour low-passed (running mean) time series (from top to bottom) of the magnitude of the wind stress, the latent heat flux, the sensible heat flux, net shortwave radiation, net longwave radiation, net heat flux, and accumulated precipitation at the five mooring sites.

Table 8
Observed seasonal and mean net heat flux (W m$^{-2}$)

| Mooring | Summer 91 | Fall 91 | Winter 91–92 | Spring 92 | Summer 92 | Fall 92 | Winter 92–93 | Spring 93 | 91–93 |
|---------|-----------|---------|--------------|-----------|-----------|---------|--------------|-----------|-------|
| NE | 78.8 | −71.8 | −25.5 | 102.1 | 101.6 | −96.4 | −59.1 | 82.4 | 14.1 |
| NW | 62.6 | −65.8 | −23.9 | 102.1 | 92.9 | −68.2 | −42.2 | 80.1 | 14.5 |
| C | 103.9 | −48.2 | −0.2 | 115.1 | 99.0 | −28.6 | −20.7 | 95.8 | 39.5 |
| SW | 89.3 | 1.1 | −33.5 | 43.3 | 50.0 | −25.6 | −14.1 | 77.8 | 23.5 |
| SE | 106.5 | −23.5 | −5.5 | 89.6 | 104.6 | −26.8 | −9.7 | 71.6 | 38.3 |

## 3.4. Freshwater flux

In general, rain provided only a small additional contribution to the buoyancy forcing in the Northeast Atlantic. From spring through summer, infrequent showers, characterized by small rain rates (peaks of ∼4 mm h$^{-1}$ and less) were observed at the buoys (Fig. 4). In the monthly fields prepared using the gridded NCEP precipitation data much of the region had average rain rates below 0.05 mm h$^{-1}$. In the fall, precipitation increased at the southern edge of the region; monthly averages along 10°N increased to ∼0.2 mm h$^{-1}$ while at SW and SE rain events remained few and rates small. In the winter, the rain along 10°N decreased again toward spring and summer values. In the northwestern half of the region, rain rates increased in the fall and winter in association with synoptic weather events (Fig. 4). These events had higher peak rain rates (up to ∼16 mm h$^{-2}$) than those seen in the spring and summer, and monthly means in the vicinity of NW reached 0.4 mm h$^{-1}$.

## 4. The thermal structure of the upper ocean in the Northeast Atlantic

### 4.1. Moored temperature data

The temperature records at the moorings (Fig. 5) showed seasonal evolution that penetrated down to roughly 100 m. Growth of a shallow seasonal thermocline in the spring and summer was followed by its erosion in the fall and winter. Underneath was a permanent thermocline where temperatures occasionally had large temporal changes (up to 2°C month$^{-1}$) with strong vertical coherence that persisted for one to several months. Neither the upper ocean nor the permanent thermocline experienced net warming or cooling over the 2 yr.

The deepest average winter mixed layer depth and largest average annual range found in monthly averaged mixed layer depths and also determined from least-squares fitting of sinusoids with an annual period (A1 sin $((2\pi/365)t + A2) + A3)$ to daily mixed layer depths were observed at C (Table 9). This fitting was done to minimize the influence of mixed layer depth transients due to eddies. Greater year-to-year variability and deeper 1-yr maxima in mixed layer depth were seen at NE and NW. The time of the deepest penetration (the shallowest mixed layers) was earliest, coming on February 22 (August 23) at NW and progressively later at NE, on February 27 (August 29), at C on March 5 (September 5), at SW on March 11 (September 11), and at SE on March 20 (September 20). SE was observed to have the shallowest winter mixed layer of any of the moorings during both winters. The monthly averaged mixed layer depths from the mooring data set were similar to those of the Levitus and Boyer (1994) climatology (Fig. 6), in which averaging in time should suppress the eddy variability. In contrast to the supposition that winter mixed layer depth might shoal to the south, the moored data did not suggest a well-defined geographical pattern in mixed layer depth (Fig. 7). A clearer spatial trend was seen in mixed layer temperature, with that at NE and NW the coldest in the winter and that at SW the warmest much of the year. The mixed layer temperature at C was close to that at SE. Thus, the winter mixed layer at C was as warm as that at SE
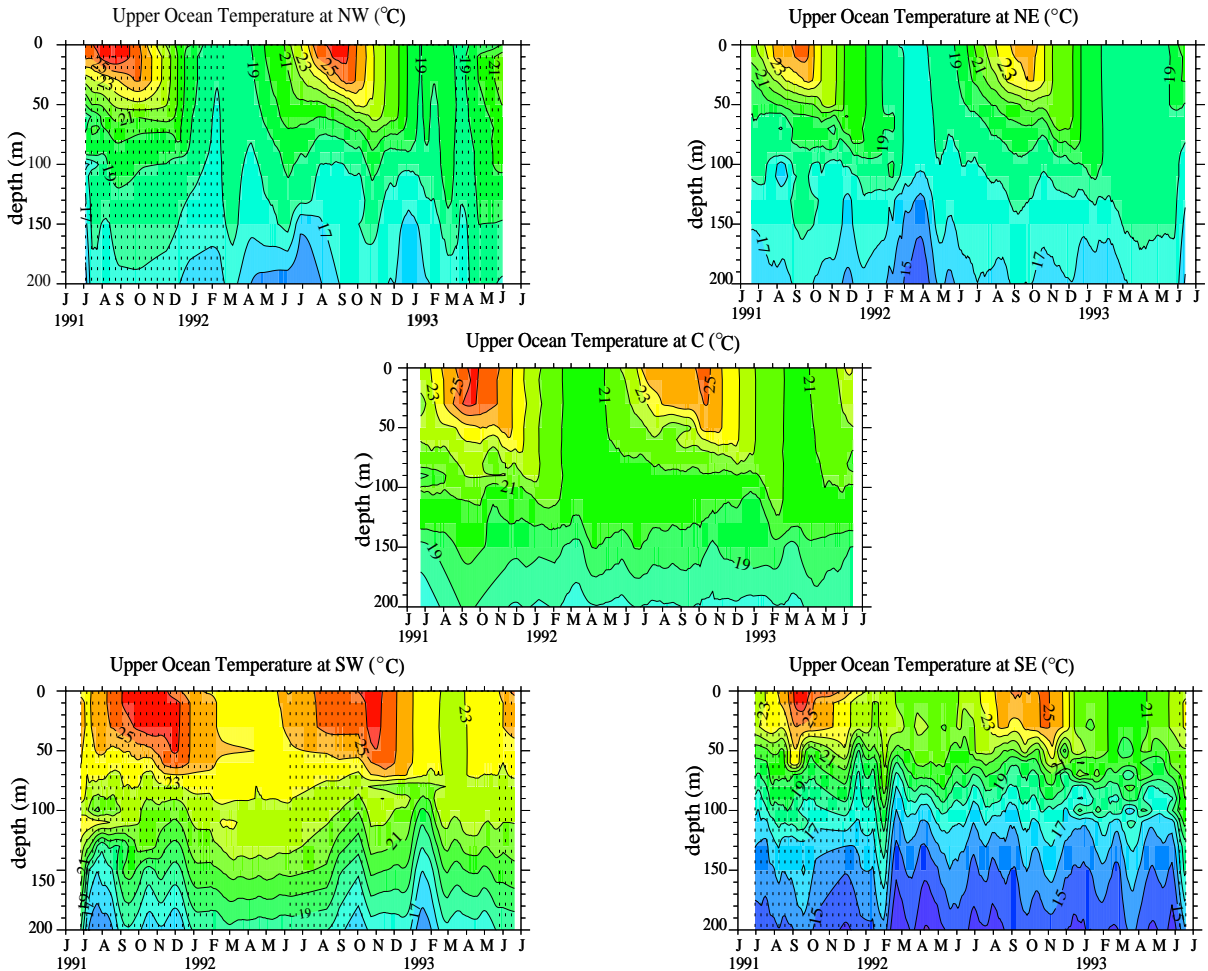
Fig. 5. Five panels, showing 2-yr contour plots of temperature at the five moorings in the upper 200 m. The temperature data from the moorings have been smoothed with a 20-day running mean, and gaps in the records at the moorings have been filled with XBT data (indicated by gray shading). One-degree contour lines are drawn.

Table 9
Minimum, maximum, mixed layer depths and annual range at moorings based on fitting a sinusoid

|    | Minimum (m) | Maximum (m) | Annual range (m) |
|----|-------------|-------------|------------------|
| NW | 4           | 109         | 105              |
| NE | 9           | 118         | 109              |
| C  | 12          | 123         | 111              |
| SW | 34          | 100         | 66               |
| SE | 14          | 54          | 40               |

while at the same time it was slightly deeper than the winter mixed layer depths at NE and NW, where the water was more than 2°C cooler.

Annual sinusoids fitted to daily averaged upper ocean temperatures at the moorings captured much of the variance at depths down to about 80 m. The annual signal contained 94% of the total variance at 10 m, but was a negligible component at 130 m. Maximum SST in the annual sinusoids lagged minimum mixed layer depth by an average of 11 days. Evident in Fig. 5 is a time delay between the warming of the upper thermocline, which continued to warm after SST had begun to cool, and of the surface layers. The warmest waters at 75 m are found 2–3 months after the warmest waters are found at the surface.
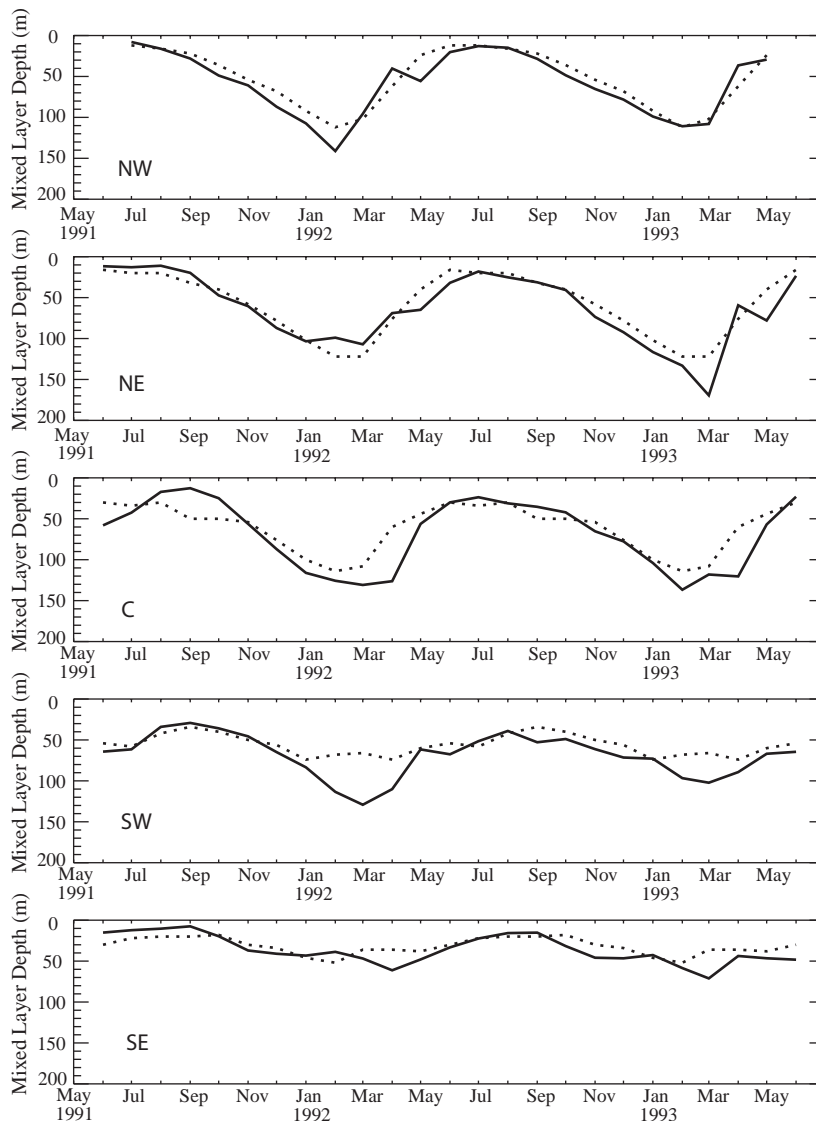
Fig. 6. Time series of the climatological monthly mean mixed layer depths at the mooring sites from the Levitus and Boyer (1994) (solid lines) repeated for 2 yr and of the monthly mean mixed layer depths observed at the moorings sites in 1991–1993 (dashed lines).

This is similar to the lag in the three-dimensional modeling study of Spall et al. (2000), in which the warmest waters at 75–100 m depth are found 3–4 months after the warmest waters are produced at the surface. Analysis of the model temperature budgets revealed that this was due to the vertical diffusion of the warm seasonal thermocline downward in late summer and early fall (Spall et al., 2000). Maximum temperature in the fitted annual

sinusoids at 60 m depth lagged the warmest surface temperatures by ∼5 weeks at NW and NE, by ∼4 weeks at C, and by ∼3 weeks at SW. The warmest near surface temperatures were observed earliest in the year at NW, about 2 weeks before those at NE, 3 weeks before those at C and SE, and 4 weeks before those at SW. While the temporal evolution of SST and mixed layer temperatures was dominated by the seasonal cycle, moored temperature
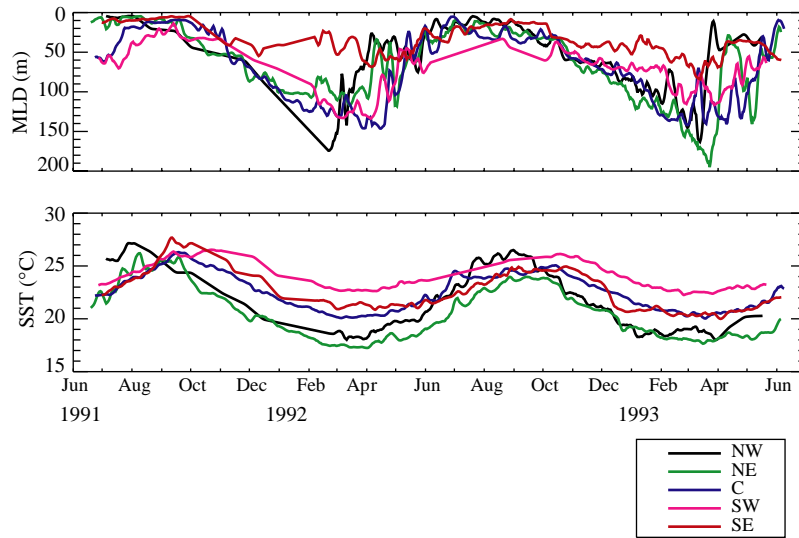
Fig. 7. Time series of mixed layer depths (upper) and mixed layer temperatures (lower) from the moorings. The time series have been low-pass filtered using a 48 h running mean.

time series from below the mixed layer and within the seasonal thermocline showed considerable variability at periods of between 5 and 100 days.

### 4.2. Spatial variability

To further examine the spatial structure of the mixed layer depth and the upper ocean temperature field in the Northeast Atlantic, climatological temperature data and the XBT data from 1991 to 1993 were examined. Monthly climatological mixed layer depths (Levitus and Boyer, 1994) in the Northeast Atlantic are deepest in February (Fig. 8), when the mixed layer depths to the north are $\sim$70 to 120 m deeper than in the south. At that time of year, a broad band of 100–130 m deep mixed layers, whose northern boundary is at $\sim$35°N and whose southern boundary runs to the southwest from the Canaries to just north of SW is seen in the climatology. To the northwest of this band, mixed layer depths increase. To the southeast of this band the isobaths of mixed layer depth shoal rapidly and are $\sim$50 m deep at SE. The shallow winter mixed layer in the southeastern sector is associated with upwelling and regional shoaling of the mixed layer south of $\sim$25°N near the African coast. In the late winter, spring, and

early summer months, the mixed layer in the Northeast Atlantic shoals, and layers deeper than 120 m disappear in March. The exception to this is a southwesterly oriented trough of 80 to 120 m deep mixed layers through the center of the region that persists during the spring. Even in May, mixed layer depths deeper than 80 m are found along in that trough, though both to the north and south, the mixed layer is shallower than 50 m. In the summer months, that trough does shoal, but remains evident (Fig. 8), with the deepest mixed layer depths to the southwest. In August the mixed layers in the trough are shallow, 20–30 m deep in the north and 40–50 m deep in the south, while outside the trough shallower mixed layers are found. Shallow, summer mixed layers persist across the Northeast Atlantic to October. In November deepening begins in the northern two-thirds of the region and then spreads further south by December, so that much of the northeast Atlantic has a climatological mixed layer depth of between 50 and 80 m. In December mixed layer depth isobaths in the southern half of the region take the west-southwesterly alignment noted in February, and in January the mixed layer depth in the upper third of the region exceeds 80 m, with a small region of mixed layers greater than 120 m.
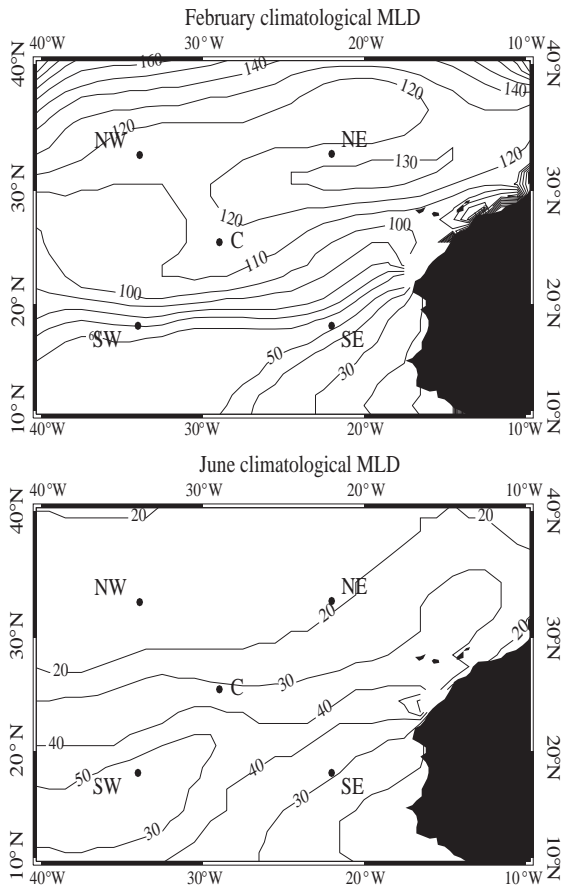
Fig. 8. Upper: Contour plot (10°–40°N, 10°–40°W) of the February climatological mixed layer depth based on the Levitus and Boyer (1994) climatology and on locating the mixed layer depth where temperature drops 0.5°C below that at the surface. Lower: contour plot of the June climatological mixed layer depth. The locations of the five moorings are shown as black dots.

The monthly climatology of the mixed layer temperature has a strong seasonal signal. The coolest temperatures are coincident with the deepest mixed layers, but the warmest temperatures lag the occurrence of the shallowest mixed layers by about a month and are seen at the end of summer and in the fall. Surface water in the southwestern part of the region is warmest throughout the year, and has the smallest annual cycle. Elsewhere, there is more variability, which is linked to change in the large-scale pattern of SST. At 40°N, the isotherms of mixed layer temperature

have a zonal orientation throughout the year. South of 40°N, however, the upwelling along the west coast of Africa leads to cooler mixed layer temperatures that extend out along the coast. In the winter and spring the upwelling results in cool, water along the African coast and isotherms within the area of array that run from northwest to southeast, with both cooler water and a larger amplitude annual signal in the northeast. In the summer the mixed layer temperature gradient in the array is dominated by a warming trend running from east to west, and the isotherms are predominantly meridional. Below the mixed layer, in the seasonal thermocline, the temperature field shows a tongue of warm water that extends from the southwest to the northeast, with its axis slightly to the northwest of C, that persists through the year. Water to both the southeast and northwest of this tongue is cooler. Evidence of this warm tongue is seen at 300 and 500 m depth. At 1000 m, however, the isotherms are zonal within the area of the array.

Two-year mean temperature fields were developed from the mooring and XBT data sets. These had large-scale spatial structure similar to that of the climatological fields. Isotherms in the contour plot (Fig. 9) of temperature at 10 m deep run northwest to southeast with the warmest water found toward the southwest. At 100 m depth a broad tongue of warmer water extended from the southwest to the east–northeast, and at 300 m the warmest water was found in the 2-yr mean field in a broad zonal band between roughly 20°N and 30°N. The seasonal variability in this data was also similar to that found in the climatological data.

To look at what spatial structure was not resolved by the moored array, the hourly XBTs taken when steaming between the mooring sites were examined. In general, the spatial variability in the surface and mixed layer temperature fields was small; fitting a linear trend to SST or mixed layer temperature along the cruise tracks removed 60% of the variance on average. The mixed layer depth along these tracks, however, showed significant mesoscale structure superimposed upon the large-scale spatial trends discussed above. As a result, linear fits to the mixed layer depths removed an average of only 22% of the variance along the
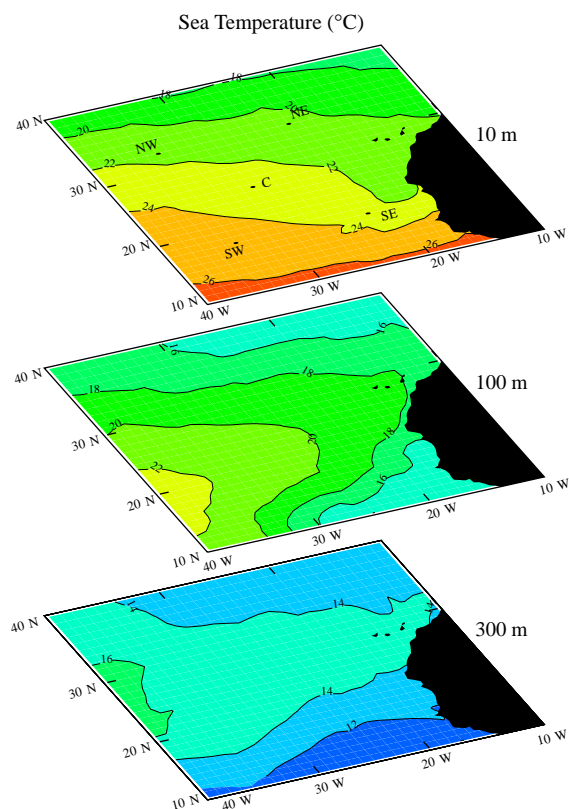
Sea Temperature (°C)



Fig. 9. Stacked contour plots of temperature at three depths (10, 100, and 300 m) of the average temperature field for June 1991 through June 1993 based on the XBTS available in the northeast Atlantic. The location of the moorings are noted on the 10 m depth contour plot.

XBT sections between moorings. The energetic 5–100-day variability in the seasonal thermocline temperatures and the mixed layer depth seen at the moorings is interpreted to result from the slow movement of mesoscale eddies through the region. It was such structure that was encountered along tracks between moorings. The amplitude of the temperature variability associated with these events was greatly diminished at 300 m, and no evidence of such variability was seen at greater depths.

## 5. Velocity structure

The 5–100-day variability seen in thermocline temperatures was associated with strong velocity

variability evident in vector stick plots of velocities at NE and C (Fig. 10), which had the most complete time series. This temporal variability in velocity was strong relative to the mean; standard deviations in the zonal and meridional components between the surface and 200 m computed from hourly averaged velocity time series were between two and six times as large as their respective means. While strong tidal (M2) and inertial peaks were found in the rotary spectra, the 5–100-day low-frequency variability was more energetic.

The velocity data showed strong vertical coherence. The first three vertical empirical orthogonal functions (EOFs) for C based on low-passed (sub-inertial) data were associated with 85%, 8% and 3% of the variance respectively. Vertical EOFs at each of the other moorings also showed vertical structure dominated by the lowest vertical modes, with between 80% and 90% of the variance in the lowest mode. These results are similar to those reported by Müller and Siedler (1992) for current meter moorings in the Northeast Atlantic deployed from 1980 to 1989. They reported strong eddy variability at periods of between 50 and 500 days and that when computing vertical EOFs at their various northeastern Atlantic sites that typically more than 70% of the variance was associated with the first EOF and 15% with the second EOF.

To create 2-yr records for all five moorings with realistic statistics and vertical structure, the gaps in these records were filled. The dominance of vertical scales large compared to the instrument spacing supported the use of linear interpolation in the vertical to fill gaps at some depths when the other depths were available. When data were missing from all depths at once, the gap was filled by copying a section of data from that same mooring, with the first choice being to use data from the same season in the other year.

Table 10 summarizes the 2-yr mean velocities. The mean velocities are consistent, in general, with the clockwise pattern of geostrophic currents in the northeast Atlantic deduced from historical hydrographic data (Fig. 1a), though the westward mean flow inferred for NW is not. The shallowest currents are rotated relative to deeper flows; they
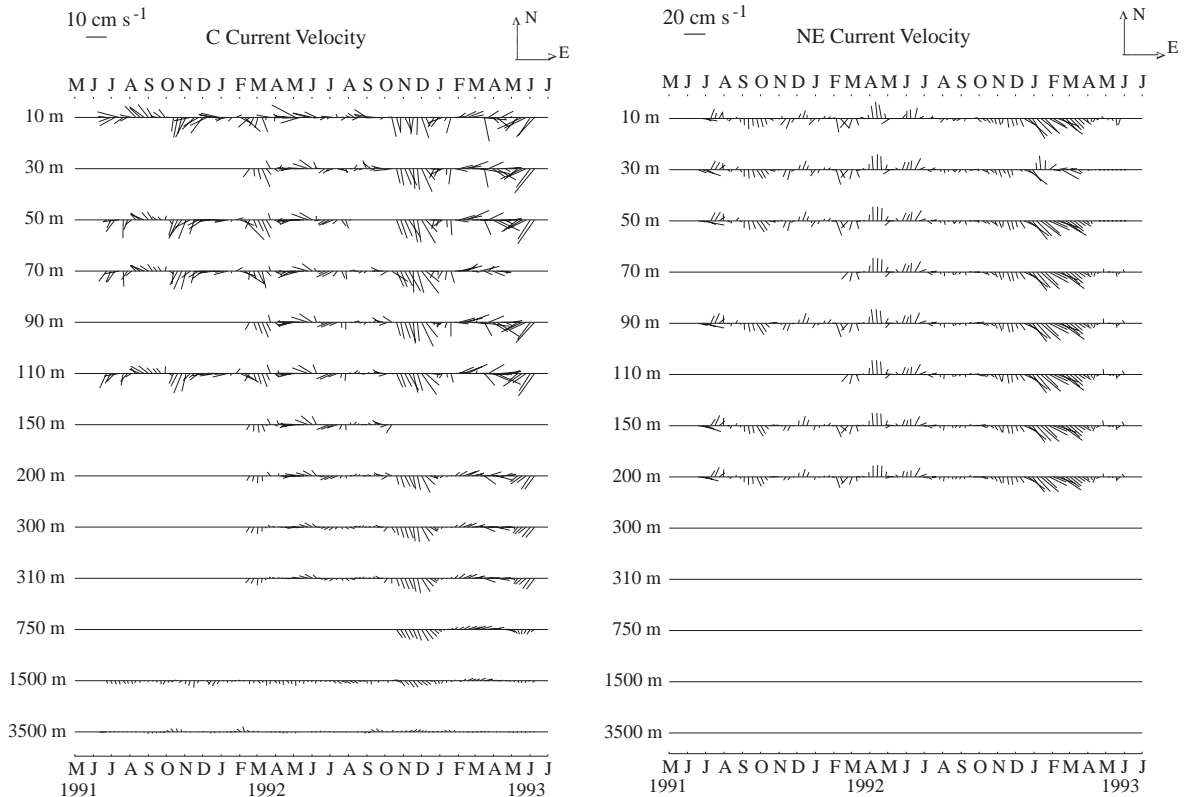
Fig. 10. Seven-day averaged velocity vectors from NE and C, with vectors drawn when data were available. No current meters were deployed at depths greater than 200 m on NE. Note the factor of 2 difference in scales, with stronger flows seen at NE. The velocity scale is shown at the top of each set of plots.

include the wind-driven surface flow which is discussed in the next section. The net flow in the mixed layer and seasonal thermocline at NE was to the southeast and that at NW was to the west. Net displacements at C in the mixed layer and seasonal thermocline were to the south–southwest. The velocity records obtained at SE show flow to the southwest in the mixed layer and to the southeast below. Surface flow at SW was to the west, and that below the mixed layer was to the southeast.

The agreement between some of the observed 2-yr means and the climatological picture of the general circulation of the northeast Atlantic may be fortuitous. As noted by Müller and Siedler (1992), Spall (1990), and others, the mean current at sites near NE is small compared to the variability and current meter records longer than

2 yr do not yield stable means. For example, at the Kiel276 site, which is close to NE, Müller and Siedler find oscillation in the zonal flow at periods of 3–4 yr. Our calculated 2-yr mean at NE is determined largely by the strong flow to the southeast observed during three of the last 6 months. However, the net contributions of the 50–100-day perturbations to the speed and direction of the accumulating mean velocity vectors at C, SE, and SW were much smaller and the presence of significant mean flow apparent in the progressive vector diagrams for those sites.

The deeper vertical array of current meters at C, where velocity was measured down to 3500 m, was used to examine the velocity in and below the thermocline. The choice of the site for the Subduction experiment had been influenced by the studies of Schott and Stommel (1978), Behringer and

Table 10
Two–year mean velocities in cm s$^{-1}$ from the filled time series. (Note: the six depths at NW are 17, 29, 48, 69, 88, and 103 m.)

| Depth | NE | NW | C | SW | SE |
|---|---|---|---|---|---|
| 10 | 3.6, −4.5 | −5.1, 0.2 | −2.9, −1.6 | −7.5, −0.2 | −8.8, −3.5 |
| 30 | 5.3, −4.2 | −4.2, 1.1 | −1.4, −2.1 | −3.2, 1.1 | −3.3, −2.2 |
| 50 | 6.0, −4.1 | −5.5, 1.5 | −0.9, −2.5 | −3.5, −3.5 | 1.7, −4.3 |
| 70 | 5.5, −3.9 | −5.2, 1.3 | −1.0, −2.3 | −3.2, −3.9 | — |
| 90 | 5.4, −3.6 | −5.8, 1.6 | −1.0, −2.1 | −3.8, −3.3 | — |
| 110 | 5.4, −3.6 | −5.7, 1.1 | −0.9, −1.7 | −3.8, −3.3 | — |
| 150 | 4.9, −3.4 | | −1.1, −1.2 | −3.7, −3.5 | — |
| 200 | 4.3, −3.2 | | −1.0, −1.2 | −1.9, −0.2 | — |
| 300 | — | | −0.7, −0.7 | — | — |
| 750 | — | | −0.2, −0.8 | — | — |
| 1500 | — | | 0.2, −0.7 | — | — |
| 3500 | — | | −0.3, 0.1 | — | — |

Stommel (1980), and others that pointed to the eastern side of the subtropical gyre as a region where Sverdrup dynamics was dominant. The velocity records at C were examined to see if the interior flow showed evidence not only of southward flow, consistent with geostrophic flow governed by Sverdrup dynamics in a region of negative wind stress curl, but also the turning with depth characteristic of the $\beta$-spiral. The hodograph of the flow at C showed the interior flow down through 1500 m toward the south–southwest, but stronger in magnitude and without the clean spiral character of that deduced from hydrographic data by Behringer and Stommel (1980). Other processes such as mixing (Olbers et al., 1985) can alter the vertical profile of horizontal velocity in the interior and may influence flow in the region.

A complementary view of the upper ocean velocity field in the Northeast Atlantic is provided by Lagrangian float data. Maillard and Kasë (1989) looked at surface drifters in the northern part of the region and estimated surface current to be 4 cm s$^{-1}$ to just south of west at NE and 7 cm s$^{-1}$ to the southwest at C. Sundermeyer and Price (1998) reported that the drift velocity of SOFAR floats deployed from 1991 to 1993 near C at depths close to 300 m and to the northeast of C at depths of 155–285 m was $(u,v = -1.2 \pm 0.3$ cm s$^{-1}$, $-0.9 \pm 0.2$ cm s$^{-1})$. The trajectories of the ALACE and bobber floats deployed roughly between and around NE and C during the experiment are shown in Fig. 11. Averaging these data over $6°$ longitude and $4°$ latitude yields the mean Lagrangian flow shown in Fig. 12. The eastward flowing Azores current is evident to the north of and between NW and NE in the trajectories and in the averaged flow field. Trajectories of floats deployed near NE move away from their deployment sites, many covering about $10°$ in 200 days ($\sim 6$ cm s$^{-1}$), but along tracks that head over diverse directions that range from westward to southeastward. The majority of these tracks are to the south and southwest, so though the mean Lagrangian velocity is small in the region between NE and C (Fig. 12), it does appear that particles do typically move away from NE toward the south and southwest.

## 6. The locally forced component

Both the velocity and temperature records collected during the Subduction Experiment from the Northeast Atlantic offer evidence that local atmospheric forcing contributes significantly to the upper ocean variability in that region. Progressive vector diagrams of the shallow flow relative to that at 50 m show the near-surface flow moving off to the right of the wind stress (Fig. 13). Rotary cross spectra of the wind stress and the vertical shear show significant coherence between the wind stress and the shear at the base of the mixed layer. Both
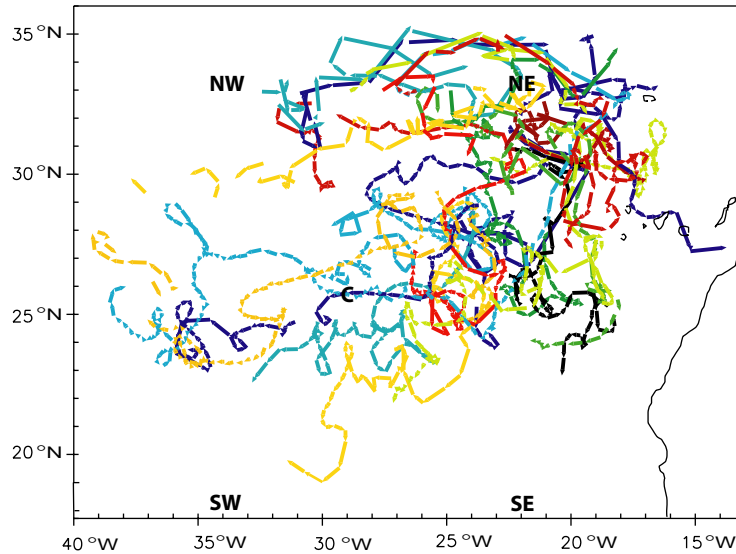
Fig. 11. Trajectories of ALACE and bobber floats deployed during the Subduction Experiment. There is one arrow for each 10-day averaged displacement.
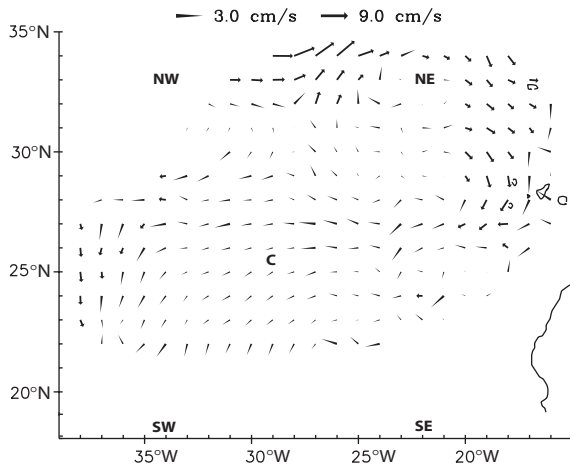


Fig. 12. The mean Lagrangian velocity field determined by averaging the data in Fig. 11 in 6° longitude by 4° latitude boxes.

findings are consistent with the presence of a wind-driven surface layer. Wind-driven transports estimated by using near- surface currents relative to those below the mixed layer agreed to within 20% of the Ekman transport estimated from the wind-stress, similar to what was found in the western part of the gyre (Price et al., 1987).

A link between the dominant seasonal variability in the thermal structure in the upper ocean in the Northeast Atlantic and the seasonal variability in the wind stress and the buoyancy flux is suggested, as spatial evolution and the timing of the mixed layer deepening and shoaling corresponds to the seasonal evolution the surface forcing and the response of the mixed layer to specific forcing events is evident, such as the warm and shallow summer mixed layer at NW that forms due to the light summer winds found there. To be more quantitative, the cumulative surface heating (time-integrated surface net heat flux) was compared with the temporal evolution of the heat content of the upper ocean, calculated from the surface down to different reference depths, and one-dimensional models were forced with the observed fluxes at the mooring sites.

Comparison of the temporal evolution of the time-integrated surface heat flux and the depth-integrated upper ocean heat content provided one way to judge the extent to which the surface heat flux alone could have caused the change in the upper ocean heat content. This comparison is shown in Fig. 14 for C, where the heat content has been computed down from the surface to various
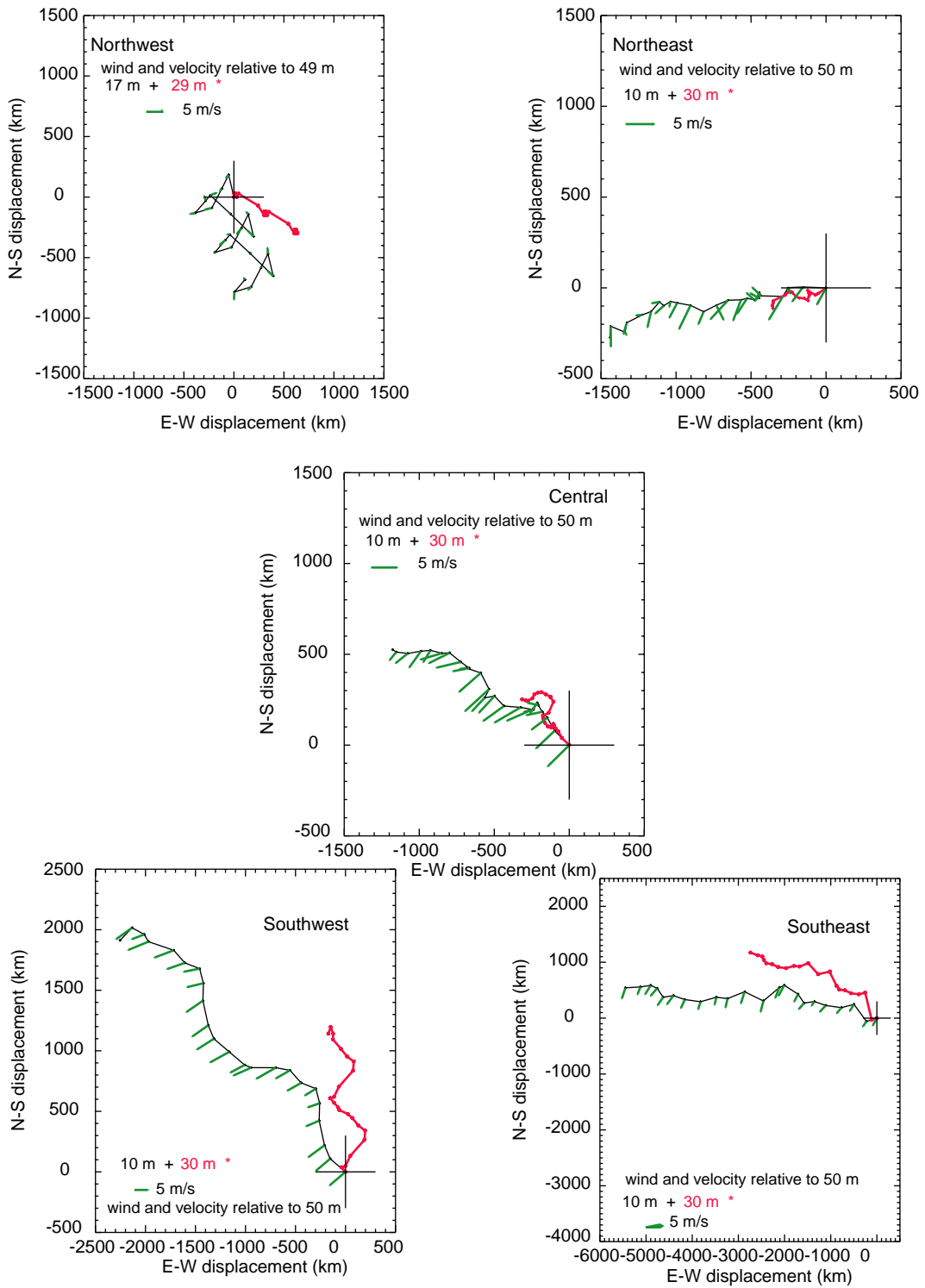
Fig. 13. Progressive vector diagrams of the flow at 10 m relative to 50 m for periods when velocity data was available. Weekly mean wind stress vectors are plotted on the provects at the mid-point of each week. The depths of the vector diagrams are color coded, and the scale for the wind stress vectors is given with the color code.
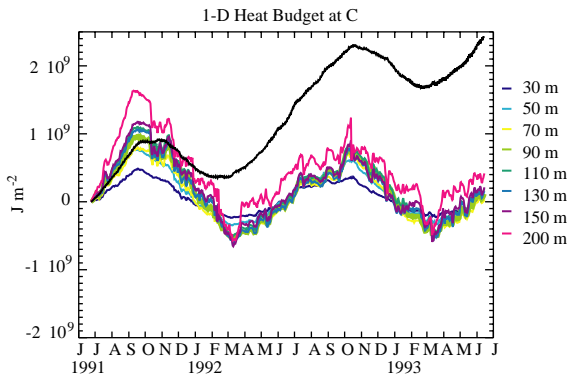
Fig. 14. For C, a comparison of the time integrated net surface heat flux (black line) against the time evolution of the upper ocean heat content computed by integrating temperature from the surface down to different depths as noted by the different colored lines. The initial points of all curves have been slid to zero at the first day of the 2-yr time series.

different depths. The seasonal cycle in upper ocean temperatures seen at the five moorings is reflected a seasonal cycle in the upper ocean heat content. However, the time-integrated surface heat flux, when set to start from zero in June 1991, ends its second annual cycle above zero, reflecting the net positive surface heating found over the Northeast Atlantic. This is not reflected in the 2-yr records of upper ocean heat content, which all end the second year with little net gain. The heat budgets are closest to one-dimensional at NE and NW; Caniaux and Planton (1998) note that in this region that surface heat flux and entrainment at the mixed layer base are the dominant terms in the mixed layer heat budget. At the other three moorings, particularly at C and at SE, local heating by surface forcing must be countered by other processes that remove heat from the upper ocean.

The surface forcing time series at each of the mooring sites were used to drive the Price–Weller–Pinkel (PWP) (Price et al., 1986) one-dimensional mixed layer model initialized at each of the mooring sites with a CTD profile taken there. (We also ran the Mellor–Yamada (1982) and K-Profile parameterization (Large et al., 1994) models but did not find significant differences from PWP.) This was done both to provide a means to compare the influence the observed

forcing would have on the ocean at the five mooring sites and to look at the consequence of enforcing a one-dimensional balance. The timing of the predicted deepening and shoaling over the seasonal cycle, including the time lag from north to south, agreed well with the observations, reinforcing the notion that the large-scale variability in surface forcing was reflected by variability in the upper ocean. The timing of shorter-lived mixing and restratification events due to surface forcing was also replicated by the model runs. At the same time, though, the model runs yielded sea surface temperatures that were warmer than observed, particularly at NE, NW, C, and SE. These surface temperatures climbed steadily; at C the final surface temperature was over $10°C$ warmer than observed. The predicted mixed layer depths across the array were too shallow in the fall and winter, with the largest differences from the observed mixed layer depth, 100 m, at C in the second winter.

Thus, though evolution of the upper ocean fields reflects the influence of local forcing, there is also evidence of variability from other sources. A wind-driven surface layer was present; and a convergent pattern of Ekman flow was found. Within the surface layer, as noted in Section 4, the temperature field had large horizontal scales, which matched those of the surface forcing, and evolved seasonally in concert with the surface forcing. At the base of the mixed layer and in the upper thermocline, there was additional mesoscale variability in temperature. The lack of net gain in mixed layer heat content in response to annual net heating of about 30 W m$^{-2}$ and the net warming found in one-dimensional model runs pointed to additional cooling process(es) that together with local forcing set mixed layer temperature.

## 7. Discussion of processes in the Northeast Atlantic with regard to subduction in the region

Our interest in subduction led us to focus on the spatial and temporal variability of the surface forcing, of the wind-driven surface flow, and of the upper ocean thermal and velocity structure. We anticipated that the region would have close to no

net heating (Fig. 1d). We also anticipated that shallower winter mixed layer depths would be found to the south, which would favor subduction. Instead, we found that all of the region was subject to net surface heating (Fig. 2d) and that in a region encompassing C and SW the winter mixed layers were as deep as at NE and NW while as warm as at SE. Fig. 15 shows the mixed layer depths and temperature encountered while dropping XBTs every hour underway between the mooring sites. There was a well-defined transition in winter mixed layer temperature encountered in the winter of 1992 just to the northeast of C while transiting

from NE to C and the southern mooring sites. The mixed layer shoals little between NE and C, yet its temperature warms 2°C as C is approached. Penetration of this warmer water into the upper thermocline was seen in the Levitus and Boyer (1994) climatology as well as in the 2-yr mean fields shown in Fig. 9. The presence of this warm water means that isotherms that outcropped during the winter near NE are never exposed to the atmosphere in the regions near C and SW. Fig. 16 composites XBT and moored temperature data from C and SW. In the first winter, a well-mixed surface layer forms at NE with a
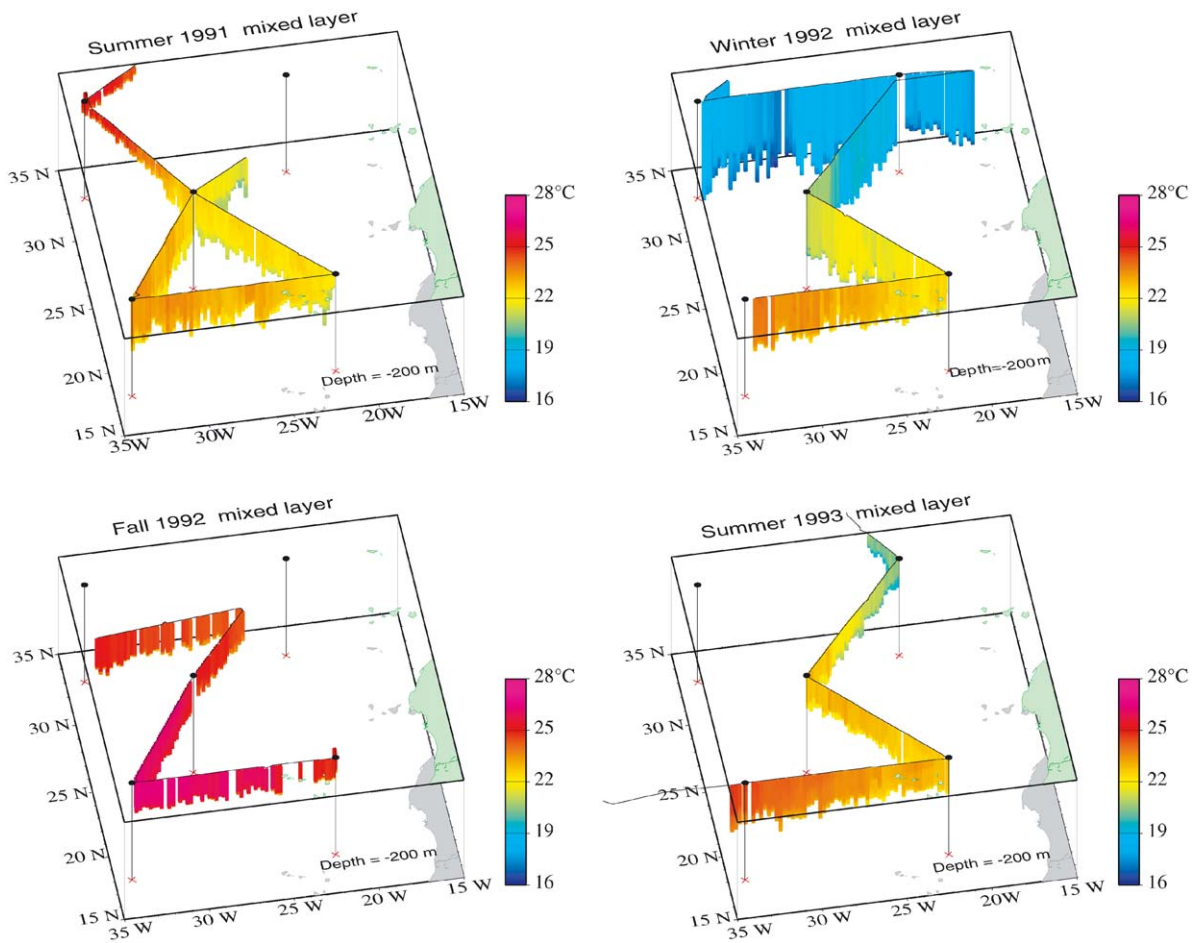


Fig. 15. Summaries of the mixed layer depth and temperature based on hourly XBT profiles taken between the mooring sites during the four cruises that serviced the moored array. Mixed layer depth (0.5°C below SST) is shown by the depth extent, relative to the 200 m full scale value, of the vertical bar, while temperature is shown by color.
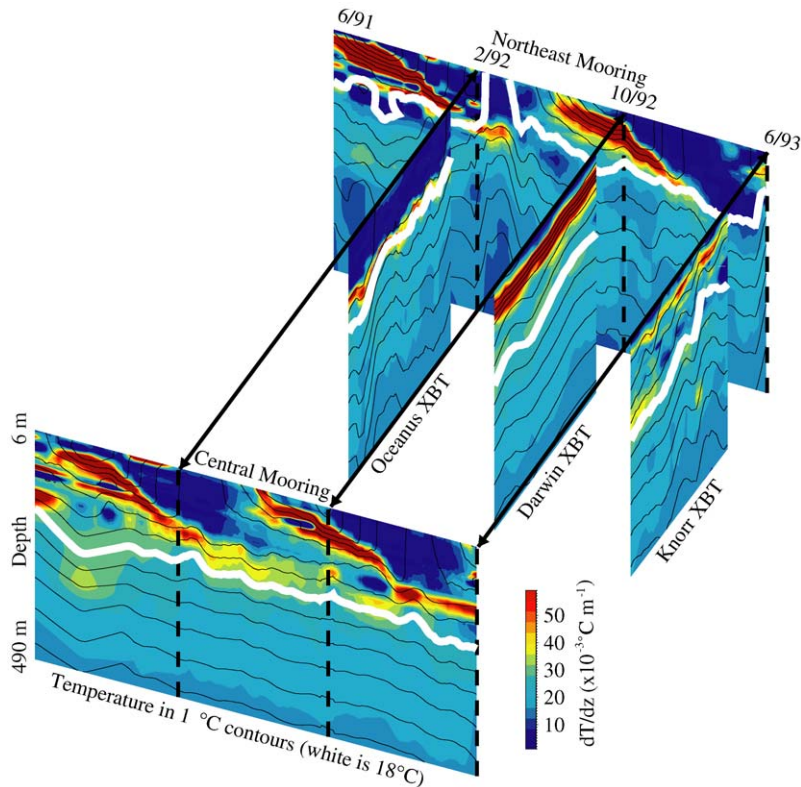
Fig. 16. Combined time/space plot of the evolution of the upper ocean temperature field from the summer of 1991 to the summer of 1993, created from mooring time series at NE and C and three ship XBT sections between C and NE. The 18°C isotherm is highlighted in white; the other whole degree isotherm depths are shown in black. The vertical temperature gradient is contoured in color.

temperature close to 18°C. The formation of the winter mixed layer and subsequent restratification also is seen at C, but there the base of the mixed layer, though as deep as at NE, penetrates down to only the 19° and 20°C isotherms. Monthly mean winter mixed layer temperatures at C and SE did not fall below 20.5°C, so that water moving down the isopycnal surfaces associated with the colder isotherms exposed during the winter to the north, such as the 18°C isotherm highlighted in Fig. 16, would not be exposed during the second winter. Water between the 18°C and 19°C isotherms is at ~150 m depth at C and then at 170 m to 200 m depth at SW (Fig. 5) indicating that if water in the upper thermocline at NE close to 18°C moves southwesterly, it moves under the warmer mixed layer, goes deeper, and is below the depth of penetration of the winter mixed layer. Thus,

the deeper but warmer mixed layer facilitates subduction.

Maintenance of the warm, deep mixed layer between C and SW is not by local air–sea interaction alone. Though $Q_{net}$ ranged from 13.9 W m$^{-2}$ at NE to 39 W m$^{-2}$ at C, there was no net warming. Ekman convergence leads to pumping of 50 m yr$^{-1}$, which deepens the mixed layer. Advection by the Ekman transport and the geostrophic flow have been pointed to in earlier work as contributors to the heat balance in the upper ocean in this region (Behringer and Stommel, 1981). Wind-driven surface flow was observed; at C, SW, and SE the wind-driven flow is to the northwest and west. The horizontal advection of heat was estimated as $\rho C_p h(u\Delta T/\Delta x, v\Delta T/\Delta y)$, using mixed layer temperature gradients between the moorings and from XBT data and a

depth, $h$, of the layer of 20 m. The value of 20 m was chosen based on analysis of the Ekman response, which showed that the mean wind-driven flow decreases rapidly with depth in the upper 50 m. The wind-driven flow is across small temperature gradients (upper panel of Fig. 9), and the estimated heat fluxes associated with the Ekman component of the flow were all less than 5 W m$^{-2}$, with cooling of the mixed layer at SE and NE, warming at C and NW, and no significant heat transport at NW due to the lack of mean wind-driven flow. The convergence of the wind-driven flow in the region at and between C and SW does, however, support the existence of the deep, relatively warm mixed layer there. The wind-driven surface flow is convergent to the northwest of the southwesterly axis of the strongest trade-winds, which is reflected in the deep mixed layers found there; the strongest mean Ekman pumping determined from the wind stress field was just south of C and at SW, with a mean of 50 m yr$^{-1}$. The large-scale geostrophic flow is likely to provide at least some of the cooling that keeps sea surface temperatures from climbing in response to the positive annual net heat flux at the sea surface. Its contribution to the heat budget near the surface was also estimated, using a mean surface layer depth of 50 m and velocities from the current meters. This flow at C, SE, and SW brought cooling, removing up to 25 W m$^{-2}$ in the winter and somewhat less in the summer when temperature gradients were smaller. At NW and NE, no estimates were made, as the mean velocities were not considered to be well defined; however, these sites were also the ones closest to being in one-dimensional balance.

It is of interest to consider the impact on subduction of the presence of the warm deep mixed layer between C and SW. Jenkins (1998) shows age gradients in $^3$H–$^3$He age on the 26.4 and 26.6 kg m$^{-3}$ isopycnals to be oriented northeast–southwest, with the youngest water found closer to the surface and in the northeast and water 2–4 yr older found roughly 100 m deeper in the southwest. If due to advection alone, the age gradient suggests velocities of $\sim 2$ cm s$^{-1}$. The Lagrangian velocities found between NE and C were $\sim 6$ cm s$^{-1}$ to the southwest. Eulerian velocities in the thermocline were $\sim 2$ cm s$^{-1}$ at C and $\sim 4$ cm s$^{-1}$ at SW. This southwestward flow along isopycnals would carry water down and under the deep warm layer found along the northwest flank of the Northeast Trades.

To better visualize the combination of the seasonal cycling of the upper ocean and the movement of water from the mixed layer into the thermocline, the time/space evolution of the temperature and salinity structure along the path of subduction through the Northeast Atlantic was examined using the GDEM (Generalized Digital Environmental Model, Teague et al., 1990) climatology. The path was chosen based on maps of dynamic height of this region and on the current meter observations made at the five mooring sites. The path goes from the northeast to the southwest, passing through NE, C, and SW, and then turns due west after reaching SW. The progression along the path was at a constant rate, taking 3 years to pass from NE to SW. Fig. 17 shows the temperature structure, with the mixed layer depth and depth of isopycnals; Fig. 18 shows the salinity structure, mixed layer depth, and isopycnals. The isopycnals descend steadily moving from NE past C and then level out, except for the seasonal cycle, between C and SW. The warming and increase in salinity of the mixed layer is apparent, and fluid descending along isopycnals such as 1027 kg m$^{-3}$ moves under the warm, salty mixed layer. The winter mixed layer seen north of C is deeper than that encountered north of NE, but the mixed layer is warmer to the south and the fluid passes underneath without being re-entrained.

The assumption of a steady progression of subducted water to the southwest might be incorrect, particularly in the northeastern part of the region, where eddy variability dominates. A profiling float launched near 27°N between NE and C in February 1992 (Fig. 19) moved as far south as 23°N, but had a net southward displacement over three years of only about 100 km ($\sim 1$ cm s$^{-1}$). However, Joyce et al.'s (1998) work to tag late winter water near NE with bobber floats and to follow these floats in subsequent cruises showed them moving to the southwest and that their sinking rate along an isopycnal was 40 m yr$^{-1}$, close to that anticipated based on the wind stress curl.
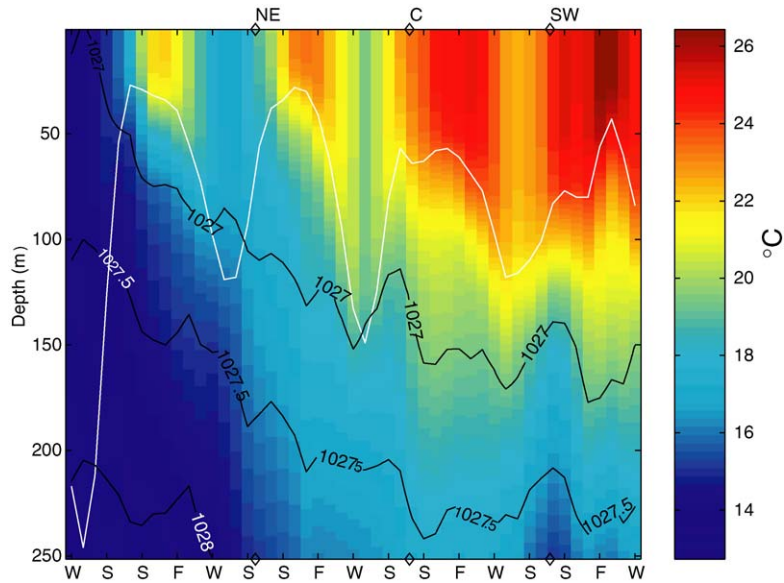
Fig. 17. A time/space section through the climatological temperature field in the Northeast Atlantic. The section is from the northeast corner of the Northeast Atlantic through NE, C, and down to SW; at SW the section continues west to 40°W. The climatology is sampled and plotted as a function of the time of year, based on moving at a rate along the section that would take 3 yr to transit from NE to SW. The mixed layer depth is shown in white; selected isopycnals are in black.
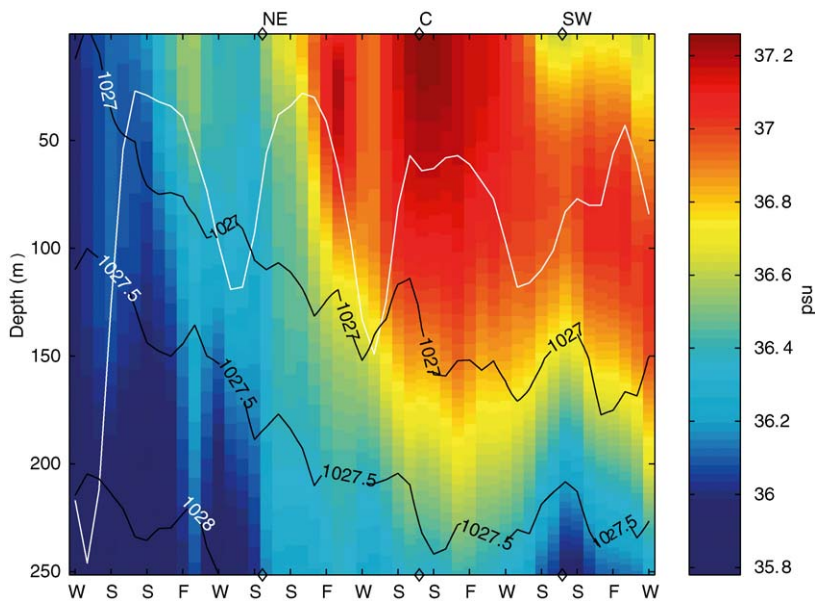


Fig. 18. A time/space section through the climatological salinity field in the Northeast Atlantic. The section is from the northeast corner of the Northeast Atlantic through NE, C, and down to SW; at SW the section continues west to 40°W. The climatology is sampled and plotted as a function of the time of year, based on moving at a rate along the section that would take 3 yr to transit from NE to SW. The mixed layer depth is shown in white; selected isopycnals are in black.
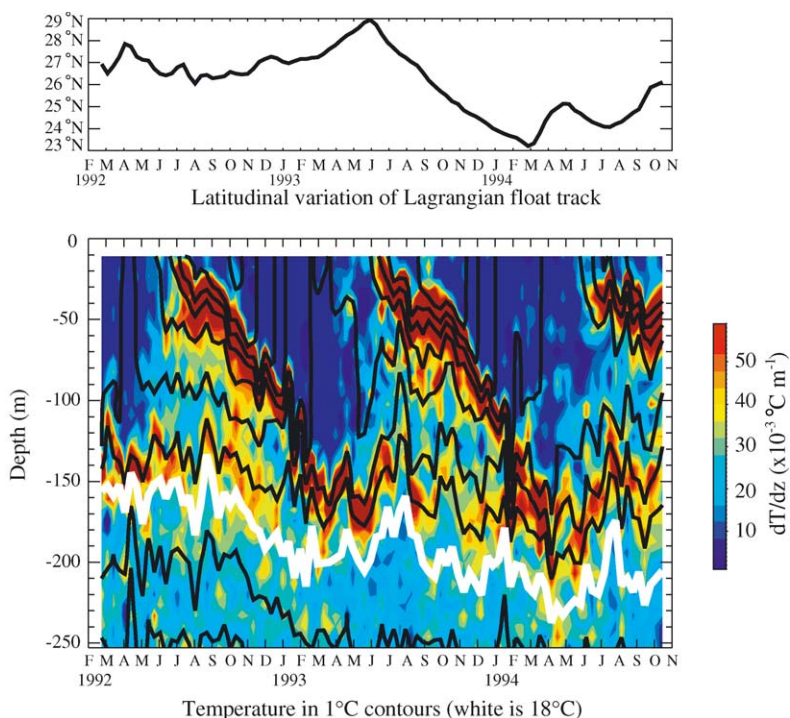
Fig. 19. Lagrangian observations of the evolution of the upper ocean temperature field from the winter of 1992 to the fall of 1994, using data from a profiling float. The latitude of the float as a function of time is shown above; the temperature data are shown below. The 18°C isotherm is highlighted in white; the other whole degree isotherm depths are in black while the vertical temperature gradient is contoured in color.

Previously, Siedler et al. (1985) had looked for evidence, in the form of mode water, for the formation at the surface of an identifiable contribution to the water in the thermocline in the eastern North Atlantic. They identified quasi-homogeneous layers with temperatures near 18°C with horizontal extents of up to 500 km in hydrographic data taken between the Azores and Canary Islands, between Madeira and the Canary Islands, and east of the Canary Islands, including near NE. They point to the outcrop of the densities associated with this water ($\sigma_t = 26.5$ to $26.8\,\mathrm{kg\,m^{-3}}$) as being located near NE. Using historical XBT profiles, they looked for other evidence of this homogeneous layer, including of it being capped over in the spring. They found that the layer with temperatures in the 17–18°C range was formed near Madeira, and named the water mass Madeira Mode Water, and that the water moved west and south from where it was formed during the spring

and summer. They did not find that it persisted beyond several months and suggested that the mode water disappeared due to mixing. Joyce et al. (1998) confirm that mixing is present, as they found the potential temperature of the water in which the bobbers they tracked were embedded decreased from 18.7°C to 18.0°C.

Since the Subduction Experiment took place, there has been additional consideration of the role of eddies in the subduction processes. Gent et al. (1995) discuss an additional transport velocity known as the eddy-induced transport velocity. Marshall (1997) presents a formula for net subduction as the sum of an Eulerian subduction contribution and of an eddy subduction contribution. The Eulerian contribution includes the processes we considered in planning our field work, Ekman pumping, lateral induction, and control of the mixed layer depth by surface forcing. The eddy subduction contribution is

non-zero if there is correlation between eddy velocities and the slope of the mixed layer base on the scale of the eddies and/or between the instantaneous Eulerian subduction rate on the scale of the eddy and the eddy horizontal scale over which it was applied. Though we do not have the data to compute ensemble averages to estimate these two terms, the current meter records point, at least, to strong correlation between mixed layer depth and eddy velocities. Thus, it is felt that the conclusion that eddy transport processes aid the transport of water from the vicinity of NE down along isopycnals is consistent with our float data, with the findings of Joyce et al. (1998), with Jenkins' (1998) age gradients, and with other investigations of Madeira Mode Water formation.

Thus, accepting that Lagrangian and Eulerian processes together carry water to the southwest from NE to SW, which is supported by the data from the floats, which respond to the mean and eddy-induced flow, Figs. 13–18 do point to a large-scale geometry for subduction in the Northeast Atlantic. Though in the north there is a strong annual cycle in mixed layer depth and temperature accompanying the annual cycle in surface forcing, the presence of persistent trade winds and seasonal variability in cloud cover reduce the latitudinal gradients in buoyancy forcing found elsewhere at the same latitudes. The convergent surface flow associated with the trade winds leads to deeper, warmer mixed layers in the central and south-western part of the region. The surface layer is sufficiently warm that it forms a buoyant cap that protects water moving from the surface in the northeastern part of the region toward the south-west and underneath and into the thermocline. In subsequent winters, the mixed layer base overhead is well above. Not so apparent, however, is whether or not the surface water from within the warm cap, roughly between C and SW, can be subducted during the year.

## 8. Conclusions

The perspective of subduction, then, that one builds for the Northeast Atlantic, is somewhat different than what was anticipated. First, it is a

region of net heat gain with less meridional gradient in the net forcing than anticipated. In contrast to the de Silva et al. (1994) climatology, the Northeast Atlantic was found to be an area of mean net heating of $\sim 30\,\text{W}\,\text{m}^{-2}$, where SE and C received about $20\,\text{W}\,\text{m}^{-2}$ more heat than NE, NW, and SW, a result supported as an improved quantification of the typical net heat flux there by Josey (2001). Seasonal variation in incoming shortwave at the top of the atmosphere and in cloud cover showed differences across the mooring sites, but such gradients were largely offset by opposing gradients in net longwave radiation and latent heat flux. Wind across the area had similar scalar speeds, though the center and southeast was dominated by steady Tradewinds blowing to the southwest, while to the north, greater temporal variability was seen as synoptic weather systems passed through.

Second, the meridional gradient in winter mixed layer depth that was anticipated was not found. In the central and southern parts of the region, surface convergence driven by the Tradewinds drives Ekman pumping that deepens the mixed layer, producing a trough of deeper layers aligned northeast to southwest. This deeper mixed layer is also warmer. The role of the local surface forcing is evident, but additional processes are at work. The upper ocean temperatures across the North-east Atlantic showed a seasonal cycle driven by surface forcing, but mixed layer depth was influenced by Ekman pumping and heat content was additionally influenced by lateral advection.

In the thermocline and below, particularly at NE and between NE and C, eddy variability was evident. Wind-driven surface flow was evident in the near-surface current meter records. Eulerian means consistent with the large-scale geostrophic flow of the gyre were found at C, SE, SW. Eddy variability dominated the moored velocity record at NE. It is believed that transport processes associated with these eddies, as suggested by Robbins et al. (2000), played an important role in moving water from the northeastern part of the region into the anticyclonic circulation of the thermocline found to the south and west.

As water moves from NE toward the southwest, the warm, deep mixed layer found at and between

C and SW provides a protective cap over cooler water, fostering its subduction. Winter- time mixed layers in the central region, while among the deepest, are never cool enough to re- entrain water subducted from sites to the north and northeast. Further, mixed layers to the southwest of C are warmer throughout the year, and water subducted in the region around C, can move to the southwest under these warmer layers and also be protected.

To a large extent, there is a regionality to the subduction process in the Northeast Atlantic that was unanticipated. The wind stress pattern of the Northeast Tradewinds produces the region of strong Ekman pumping together with the Ekman flow provides the warm cap over water moving to the southwest in the thermocline below. The role of the Ekman convergence has been discussed in McLaren and Williams (2001) and Marshall et al. (1993). This points to the region along the north-west flank of the Northeast Tradewinds as a location where subduction is likely to occur. We did not find that over the whole region that the observed Eulerian flow alone was sufficient to explain how subducted water was carried down along isopycnals to the southwest. In particular, near NE, where the Ekman is weaker and where no stable Eulerian velocities were found in the thermocline, we conclude that eddy-induced contributions to the subduction process are important.

In future work we would look toward more explicit consideration of the eddies and of the spatial gradients and processes associated with mesoscale variability. The NCAR Community System Model (CSM) we also used (Spall et al., 2000) to investigate subduction included the Gent and McWilliams (1990) parameterization of eddy-induced transports, and it was largely successful at replicating the monthly mean mixed layer depths and monthly mean sea surface temperatures found at the five moorings. The parameterized eddy fluxes contributed to subduction throughout the region, with the largest effect near NE, about $10 \, \text{m} \, \text{yr}^{-1}$. In a future field study, we would also deploy Lagrangian floats in densities sufficient to examine the contributions to eddy- induced subduction suggested by Marshall (1997).

## Acknowledgements

## Appendix A

Clear sky incoming shortwave time series were calculated as a function of true solar time using formulae from the Smithsonian Meteorological Tables (List, 1984). A transmission coefficient of 0.75 was chosen based on the incoming shortwave time series at the moorings. Fifteen-minute clear sky incoming shortwave values were then multiplied by the ratio of the ECMWF 6-h average and the corresponding average of the clear sky incoming shortwave. Net shortwave was calculated using the albedo of Payne (1972), a function of both solar altitude and atmospheric transmittance. Measured incoming longwave radiation was reduced by 3.6% of the incoming shortwave as suggested by Alados-Arboledas et al. (1988). Gaps

in incoming longwave were filled using clear sky longwave and a cloud correction factor (Fung et al., 1984). Clear sky longwave radiation was computed from sea surface temperature, air temperature, and near surface humidity (Clark et al., 1974). Daytime cloud cover was estimated as a function of theoretical clear sky incoming shortwave (List, 1984) and actual incoming shortwave using the cloud factor formulation of Kimball (1928). The time series of cloud cover was subsequently filtered using a 30 h running mean to provide a continuous day and night representation of cloud cover. Outgoing longwave was computed using the Stefan-Boltzmann Law and an emissivity of 0.97.

## Appendix B

Offsetting biases in the four flux components have been found to cancel (Moyer and Weller, 1997), and the estimated error in the net heat flux is less than the sum of the errors of the four components. The uncertainty in the rain gauges is based on results from TOGA COARE (Bradley and Weller, 1997). Uncertainties are summarized in Table 11.

The model data used in the comparisons with the buoy data came from the ECMWF T106/L19 model during the initial 3 months of the Subduction experiment and the ECMWF T213/L31 (ECMWF Technical Attachment, 1994) model thereafter and also from the NCEP T126/L28 model (Kanamitsu, 1989; Kanamitsu et al., 1991). The basic observables were available at 0, 6, 12, 18 UTC, and the model fluxes were available as accumulated values over an initial 6 h forecasts from which 6 hour averages were subsequently computed.

The mean wind stress forecasts of the two models differ by less than $0.006 \, \text{N m}^{-2}$ across the array. The mean wind stress from the buoys differs from the model forecasts by less than $0.005 \, \text{N m}^{-2}$ (8%) across the northern buoys, but differs by $0.013–0.020 \, \text{N m}^{-2}$ (14–19%) across the southern buoys (Table 12). The smaller model wind stresses are primarily the results of the smaller mean wind speeds within the ECMWF and NCEP analyses as

Table 11
Uncertainties in air–sea flux time series at the Subduction moorings

| Flux | Units | Error |
| --- | --- | --- |
| Latent | $\text{W m}^{-2}$ | $12–17 \pm (5–7)$ |
| Sensible | $\text{W m}^{-2}$ | $2–2.5 \pm (0.3–0.5)$ |
| net SW | $\text{W m}^{-2}$ | $5–7$ |
| net LW | $\text{W m}^{-2}$ | $15–20$ |
| net Heat | $\text{W m}^{-2}$ | $15–25$ |
| Stress | $\text{N m}^{-2}$ | $0.007–0.0100$ |
| Precip | $\%$ | $20$ |

the buoy winds exceeded the model winds by less than $0.2 \, \text{m s}^{-1}$ in the north, but by $0.5–0.7 \, \text{m s}^{-1}$ in the south. The peak in the frequency distribution curve of wind speed from the models is more pronounced than that from the buoys, with the buoys showing more occurrences of higher wind speeds. The overspeeding of the VAWR's cups explains a significant fraction of the observed discrepancies between the model and mooring wind speeds as the 6% overspeeding associated with them (Weller et al., 1990) results in biases of $0.3–0.5 \, \text{m s}^{-1}$ and $0.007–0.010 \, \text{N m}^{-2}$ in wind speed and wind stress, respectively, at typical observed wind speeds. A smaller additional difference is associated with the correction of the 3 m buoy winds to match the 10 m height of the models. Thus, the ECMWF wind stresses appeared reasonable; and they were used without correction in the gridded forcing fields. To do so the model's zonal and meridional stress components were first bilinearly interpolated onto a regular $1°$ grid. Total wind stress was then computed from these gridded components, and both total stress and the stress components were linearly interpolated to 1 hour sampling.

The mean sensible heat flux losses forecast by the models were greater than the those at the buoys. The mean sensible heat losses of the ECMWF model exceed those of the buoys by $2.5–6.2 \, \text{W m}^{-2}$ (39–132%), even though the buoy mean winds were higher and the mean air-sea temperature differences from the buoys and the ECMWF model differed by less than $0.05°\text{C}$ at four of the five moorings. The NCEP sensible heat losses were even larger than those of the buoys,

Table 12
Mean air–sea flux values from the buoys, ECMWF forecast model, and the derived gridded product

| Site | Source | Wind stress $(N\,m^{-2})$ | Sens. heat flux $(W\,m^{-2})$ | Latent heat flux $(W\,m^{-2})$ | Net SW flux $(W\,m^{-2})$ | Net LW flux $(W\,m^{-2})$ | Net heat flux $(W\,m^{-2})$ |
|------|--------|-------------|------------|--------------|-------------|-------------|--------------|
| NE | Buoy | 0.074 | −9.2 | −97 | 186 | −66 | 14 |
|    | ECMWF | 0.074 | −12.8 | −109 | 200 | −74 | 4 |
|    | Gridded | 0.073 | −7.0 | −95 | 201 | −74 | 25 |
| NW | Buoy | 0.077 | −6.5 | −92 | 186 | −74 | 14 |
|    | ECMWF | 0.067 | −8.9 | −101 | 206 | −73 | 23 |
|    | Gridded | 0.079 | −5.4 | −94 | 196 | −74 | 22 |
| SW | Buoy | 0.083 | −4.4 | −127 | 216 | −61 | 23 |
|    | ECMWF | 0.078 | −10.9 | −137 | 227 | −69 | 33 |
|    | Gridded | 0.076 | −4.5 | −121 | 224 | −67 | 31 |
| SE | Buoy | 0.098 | −7.1 | −103 | 200 | −51 | 38 |
|    | ECMWF | 0.085 | −11.2 | −119 | 219 | −62 | 28 |
|    | Gridded | 0.082 | −5.6 | −110 | 216 | −64 | 36 |
| C | Buoy | 0.073 | −6.3 | −106 | 212 | −61 | 39 |
|   | ECMWF | 0.064 | −11.6 | −121 | 212 | −73 | 7 |
|   | Gridded | 0.063 | −6.2 | −104 | 213 | −73 | 31 |

The temporal averaging for this comparison varies buoy to buoy and only includes those times when the buoys are on station. Positive values indicate oceanic heat gain.

with differences of 5.1–13.5 W m$^{-2}$ (70–280%), in part perhaps because of a 1.0–1.8°C cool bias in 2 m NCEP air temperature. Unlike the mean sensible heat fluxes, the mean latent heat fluxes from the two models agreed well with one another. However, both models' mean latent heat losses were 7–20 W m$^{-2}$ (5–25%) larger than those from the buoys. Once again, the models' larger heat losses are not consistent with the models' having lower wind speeds and, at four of the five buoys, smaller (i.e., up to 0.4 g kg$^{-1}$) interfacial moisture gradients.

It was concluded that the bulk parameterization schemes of both models lead to overestimation of the mean sensible and latent heat losses in the Subduction region. In contrast, the long- term means of the basic observables from the ECMWF model were in good agreement with those measured at the buoys locations. Both the mean sea and air temperatures from the ECMWF model and the buoys agreed to within 0.2°C, while their mean specific humidities at a height of 2 m agreed

within 0.3 g kg$^{-1}$. Thus, it was decided to compute new sensible and latent heat fluxes that would be in better agreement with those from the buoys. Thus was done by using the basic observables from the 6 h ECMWF analyses together with version 2.5 of the COARE bulk formulae to compute new fluxes.

Prior to doing so the basic observables were interpolated onto the 1° grid. Specific humidity was determined from the ECMWF sea level pressure and 2 m dew point temperature using a variation of Teten's formula (Buck, 1981). The model's utilization of a 7 day running mean sea surface temperature (Reynolds, 1991) coupled with a 12 h delay in its assimilation of the most recent sea surface temperature data results in a time lag of 4 days in the model's representation of sea surface temperature. To counter this lag, the sea surface temperature data utilized at any given time within the gridded fields was the model sea surface temperature dated 4 days into the future. No corrections were applied to the model SST to account for departures from a true skin

temperature. The potential error associated with using 6-h values in the bulk formulae was explored by contrasting sensible and latent heat fluxes computed from 15 min and 6 h sampled buoy time series. Reducing the sampling rate to 6 h produced changes of less than $1 \, W \, m^{-2}$ in the mean heat fluxes over the 2 yr deployment. Thus, sensible and latent heat fluxes were computed at the grid points using 6 h data and the COARE bulk formula and then interpolated to 1 h sampling. These sensible and latent heat fluxes agreed well with the buoys (Table 11). The new sensible and latent heat fluxes differed from the buoys by $0.1–2.3 \, W \, m^{-2}$ (2–28%) and $2–10 \, W \, m^{-2}$ (2–8%), respectively.

Mean differences in the net shortwave radiation from the buoys and ECMWF showed ECMWF to have more net shortwave at all sites except C where the means were equal. The greatest difference was seen at NW (14%), but the mean difference over the five sites was 7% (Table 12). The mean net shortwave fluxes forecast by the NCEP model agreed within 7% at three of the buoys, but at C and SW the NCEP model net shortwave was $27 \, W \, m^{-2}$ (12%) and $37 \, W \, m^{-2}$ (17%) lower, respectively. Thus, the ECMWF net shortwave was interpolated to a $1°$ grid, and the 1 h time series was created as described in the Section 2.

The mean longwave losses from both models exceeded the buoy values by $2–16 \, W \, m^{-2}$ or 3–35% with the greatest differences observed at SE. Although the forecast models appear to overestimate the net longwave loss at the buoy locations, the buoy pyrgeoemeters do have a sizable potential error of 5% ($15–20 \, W \, m^{-2}$). ECMWF net longwave forecasts were regridded to the $1°$ grid.

The buoys, the ECMWF forecasts, and the gridded product all showed net oceanic heat gain at each of the five buoys. The net heat flux of the new gridded product showed differences of between 2 and $11 \, W \, m^{-2}$ (6–44%) from the buoys, less than the $9–22 \, W \, m^{-2}$ (28–70%) difference between the buoys and ECMWF. Compared to the buoys, the gridded product had larger heat gains across the northern moorings and smaller heat gains across the southern moorings.

The freshwater flux was also calculated on the $1°$ grid. Hourly gridded evaporation rates were computed from the latent heat fluxes. The precipitation data from the NCEP model, which is an accumulation over 6 h, was bilinearly interpolated onto the $1°$ grid and then divided by 6 to get hourly rainfall rates, constant over that 6 h interval. Gaps in the NCEP precipitation data set, typically 6–12 hs in length, but totaling 40 days over the 2 yr period, were assigned a zero precipitation rate. Comparison with the buoys suggested that the NCEP model overforecasts the frequency of minor precipitation events. This tendency of the model was further exaggerated by the bilinear interpolation process. To reduce the frequency of light rain events, a precipitation threshold of $0.02 \, mm \, h^{-1}$ was established. This reduced the frequency of events to match the buoys, but changed the long-term mean accumulated precipitation little. The precipitation is used in the COARE algorithm to add in the heat flux due to precipitation by assuming that the temperature of the rain is the wet bulb temperature. This contributes approximately $0.3 \, W \, m^{-2}$ to the net heat flux annually, but can be up to two orders of magnitude larger when it is raining.

The buoyancy flux was computed as $g[((\alpha Q_{net})/c_{pw}\rho)) + (S\beta(E–P)]$, where $g = 9.8 \, m \, s^{-2}$, $\alpha$ and $\beta$ are the thermal and haline expansion coefficients, $Q_{net}$ is the net heat flux, $c_{pw} = 3996 \, J \, kg^{-1} \, K^{-1}$ and $\rho = 1024 \, kg \, m^{-3}$ are the specific heat and density of sea water at a mean temperature of $22°C$ and salinity of 35 psu, $S$ is salinity and $(E–P)$ is the evaporation rate minus the precipitation rate. Surface salinity was approximated as a function of ECWMF sea surface temperature with the aid of T–S relationships which were unique to each grid point across the array. These relationships between sea surface and salinity were derived from monthly climatological sea surface temperature and salinity data of the World Ocean Atlas, 1994 (WOA-94, 1994) which were available at a grid spacing of $1°$. A quadratic polynomial was least-squares fit to the 12 months of climatological data at each grid point through the array. Thus, at each grid point there was an equation for sea surface salinity at the sea surface temperature prescribed by ECMWF.

# References

Alados-Arboledas, Vida, L.J., Jimenez, J.I., 1988. Effects of solar radiation on the performance of pyrgeometers with silicon domes. Journal of Atmospheric and Oceanic Technology 5, 666–670.

Behringer, D.W., Stommel, H., 1980. The beta spiral in the North Atlantic subtropical gyre. Deep-Sea Research 27A, 225–238.

Behringer, D.W., Stommel, H., 1981. Annual heat gain of the tropical Atlantic computed from subsurface ocean data. Journal of Physical Oceanography 11, 1393–1398.

Bolton, D., 1980. The computation of equivalent potential temperature. Monthly Weather Review 108, 1046–1053.

Bradley, E.F., Weller, R.A., 1997. Fourth Workshop of the TOGA COARE Air–Sea Interaction (Flux) Working Group. UCAR/TCIPO, UCAR Communications, CO, USA.

Brink, N.J., Moyer, K.A., Trask, R.P., Weller, R.A., 1995. The Subduction Experiment: Mooring Field Program and Data Summary. Woods Hole Oceanographic Institution, Woods Hole, USA, WHOI-95-08, 113pp.

Buck, A.L., 1981. New equations for computing vapor pressure and enhancement factor. Journal of Applied Meteorology 20, 1527–1532.

Caniaux, G., Planton, S., 1998. A three-dimensional ocean mesoscale simulation using data from the SEMAPHORE experiment. Mixed layer heat budget. Journal of Geophysical Research 103 (C11), 25099–25801.

Clark, N.E., Eber, L., Laurs, R.M., Renner, J.A., Saur, J.F.T., 1974. Heat exchange between ocean and atmosphere in the eastern North Pacific for 1961–1971. NOAA Technical Report, NMFS SSRF-682, National Oceanic and Atmospheric Administration, US Department of Commerce, Washington, DC.

da Silva, A., Young, C.C., Levitus, S., 1994. Atlas of surface marine data, 1994. NOAA Atlas NESDIS 6, 83pp.

Davis, R.E., Webb, D.C., Regier, L.A., Dufour, J., 1992. The autonomous Lagrangian circulation explorer (ALACE). Journal of Atmospheric and Oceanic Technology 9, 264–285.

ECMWF Technical Attachment, 1994. The description of the ECMWF/WCRP level III-A global atmospheric data archive. European Centre for Medium Range Weather Forecasts, Reading, UK, 72pp.

Fairall, C.W., Bradley, E.F., Godfrey, J.S., Wick, G.A., Edson, J.B., Young, G.S., 1996a. Cool skin and warm layer effects on sea surface temperature. Journal of Geophysical Research 101, 1295–1308.

Fairall, C.W., Bradley, E.F., Rogers, D.P., Edson, J.B., Young, G.S., 1996b. Bulk parameterization of air–sea fluxes for TOGA COARE. Journal of Geophysical Research 101, 3747–3764.

Fung, I.Y., Harrison, D.E., Lacis, A.A., 1984. On the variability of the net longwave radiation at the ocean surface. Reviews of Geophysics and Space Physics 22, 177–193.

Gent, P.R., McWilliams, J.C., 1990. Isopycnal mixing in ocean circulation models. Journal of Physical Oceanography 20, 150–155.

Gent, P.R., Willebrand, J., MacDougall, T.J., McWilliams, J.C., 1995. Parameterizing eddy-induced tracer transports in ocean circulation models. Journal of Physical Oceanography 25, 463–474.

Huang, R.X., 1989. On the three-dimensional structure of the wind-driven circulation in the North Atlantic. Dynamics of Atmospheres and Oceans 15, 117–159.

Hosom, D.S., Weller, R.A., Payne, R.E., Prada, K.E., 1995. The IMET (Improved Meteorology) ship and buoy systems. Journal of Atmospheric and Oceanic Technology 12, 527–540.

Iselin, C.O'D., 1939. The influence of vertical and lateral turbulence on the characteristics of waters at mid-depths. Transactions of the American Geophysical Union 20, 414–417.

Isemer, H.-J., Hasse, L., 1985. The Bunker Climate Atlas of the North Atlantic Ocean. Vol. 1. Observations. Springer, New York, 218pp.

Jenkins, W.J., 1998. Studying subtropical thermocline ventilation and circulation using tritium and $^3$He. Journal of Geophysical Research 103, 15817–15831.

Josey, S.A., 2001. A comparison of ECMWF, NCEP/NCAR and SOC surface heat fluxes with moored buoy measurements in the subduction region of the North-East Atlantic. Journal of Climate 14 (8), 1780–1789.

Joyce, T.M., Luyten, J.R., Kubryakov, A., Bahr, F.B., Pallant, J.S., 1998. Meso- to large- scale structure of subducting water in the subtropical gyre of the eastern North Atlantic Ocean. Journal of Physical Oceanography 28, 40–61.

Kanamitsu, M., 1989. Description of the NMC global data assimilation and forecast system. Weather Forecasting 4, 335–342.

Kanamitsu, M., Alpert, J.C., Campana, K.A., Caplan, P.M., Deaven, D.G., Iredell, M., Katz, B., Pan, H.-L., Sela, J., White, G.H., 1991. Recent changes implemented into the global forecast system at NMC. Weather Forecasting 6, 425–435.

Kimball, H.H., 1928. An amount of solar radiation that reaches the surface of the earth on the land and on the sea and methods by which it is measured. Monthly Weather Review 56, 393–399.

Large, W.G., McWilliams, J.C., Doney, S.C., 1994. Oceanic vertical mixing: a review and a model with a nonlocal boundary layer parameterization. Reviews of Geophysics and Space Physics 32, 363–403.

Leetmaa, A., Bunker, A.F., 1978. Updated charts of the mean annual wind stress, convergences in the Ekman layers, and Sverdrup transports in the North Atlantic. Journal of Marine Research 36, 311–322.

Levitus, S., Boyer, T.P., 1994. World Ocean Atlas 1994. Volume 4. Temperature. NOAA Atlas NESDIS 4, US Department of Commerce, Washington, DC, 117pp.

Levitus, S., Burgett, R., Boyer, T.P., 1994. World Ocean Atlas 1994. Volume 3. Salinity. NOAA Atlas NESDIS 3, US Department of Commerce, Washington, DC, 99pp.

List, R.J., 1984. Smithsonian Meteorological Tables. Smithsonian Institution Press, Washington, DC, 572pp.

Luyten, J.R., Pedlosky, J., Stommel, H., 1983. The ventilated thermocline. Journal of Physical Oceanography 13, 292–309.

Maillard, C., Kasë, R., 1989. The near-surface flow in the subtropical gyre south of the Azores. Journal of Geophysical Research 94, 16133–16140.

Marshall, D., 1997. Subduction of water masses in an eddying ocean. Journal of Marine Research 55, 201–222.

Marshall, J.C., Nurser, A.J.G., Williams, R.G., 1993. Inferring the subduction rate and period over the North Atlantic. Journal of Physical Oceanography 23, 1315–1329.

McLaren, A.J., Williams, R.G., 2001. Interannual variability in the thermodynamics of subduction over the North Atlantic. Journal of Physical Oceanography 31, 3284–3294.

Mellor, G.L., Yamada, T., 1982. Development of a turbulence closure model for geophysical fluid problems. Reviews of Geophysics and Space Physics 20, 1315–1329.

Montgomery, R.B., 1938. Circulation in upper layers of southern north Atlantic deduced with use of isentropic analysis. Papers in Physical Oceanography and Meteorology, V. VI, No. 2, Massachusetts Institute of Technology and Woods Hole Oceanographic Institute, 55pp.

Moyer, K.A., Weller, R.A., 1997. Observations of surface forcing from the Subduction Experiment. A comparison with global model products and climatological data sets. Journal of Climate 10, 2725–2740.

Müller, T.J., Siedler, G., 1992. Multi-year time series in the eastern North Atlantic Ocean. Journal of Marine Research 50, 63–98.

Olbers, D.J., Menzel, M., Willebrand, J., 1985. The inference of North Atlantic circulation patterns from climatological hydrographic data. Reviews of Geophysics 23, 313–356.

Paillet, J., Ahran, M., 1996. Shallow pycnoclines and mode water subduction in the eastern North Atlantic. Journal of Physical Oceanography 26, 96–114.

Payne, R.E., 1972. Albedo of the sea surface. Journal of Atmospheric Science 29, 959–970.

Pingree, R.D., Sinha, B., 1999. Position and structure of the subtropical/Azore front region from combined Lagrangian and remote sensing (IR/altimeter/SeaWiFS) measurements. Journal of the Marine Biological Association of the United Kingdom 79 (5), 769–792.

Pollard, R.T., Regier, L.A., 1992. Vorticity and vertical circulation at an ocean front. Journal of Physical Oceanography 22, 609–625.

Price, J.F., 1996. Bobber floats measure currents' vertical component in the Subduction Experiment. Oceanus 39 (1), 26.

Price, J.F., Weller, R.A., Pinkel, R., 1986. Diurnal cycling: observations and models of the upper ocean response to diurnal heating, cooling, and wind mixing. Journal of Geophysical Research 91 (C7), 8411–8427.

Price, J.F., Weller, R.A., Schudlich, R.R., 1987. Wind-driven ocean currents and Ekman transport. Science 238, 1534–1538.

Qiu, B., Huang, R.X., 1995. Ventilation of the North Atlantic and North Pacific. Subduction versus obduction. Journal of Physical Oceanography 25, 2374–2390.

Reynolds, R.W., 1991. A new global sea surface temperature analysis. Technical Procedure Bulletin, Number 393. Available form the National Weather Service, Office of Meteorology, Silver Spring, MD.

Robbins, P.E., Price, J.F., Owens, W.B., Jenkins, W.J., 2000. The importance of lateral diffusion for the ventilation of the lower thermocline in the subtropical North Atlantic. Journal of Physical Oceanography 30, 67–89.

Rudnick, D.L., 1996. Intensive surveys of the Azores Front. 2. Inferring the geostrophic and vertical velocity fields. Journal of Geophysical Research 101 (C7), 16291–16303.

Rudnick, D.L., Luyten, J.R., 1996. Intensive surveys of the Azores Front 1. Tracers and dynamics. Journal of Geophysical Research 101 (C1), 923–939.

Schott, F., Stommel, H., 1978. Beta spirals and absolute ocean velocities in different oceans. Deep-Sea Research 25, 961–1010.

Siedler, G., Kuhl, A., Zenk, W., 1985. The Madeira mode water. Journal of Physical Oceanography 17, 1561–1570.

Spall, M., 1990. Circulation in the Canary Basin. A model/data analysis. Journal of Geophysical Research 95 (C6), 9611–9628.

Spall, M.A., Weller, R.A., Furey, P., 2000. Modeling the three-dimensional upper ocean heat budget and subduction rates during the subduction experiment. Journal of Geophysical Research 105, 26151–26166.

Stommel, H., 1979. Determination of the watermass properties pumped down from the Ekman layer to the geostrophic flow below. Proceedings of the National Academy of Science, US 76, 3051–3055.

Sundermeyer, M.A., Price, J.F., 1998. Lateral mixing and the North Atlantic Tracer release Experiment. Observations and numerical simulations of Lagrangian particles and a passive tracer. Journal of Geophysical Research 103 (C10), 21481–21497.

Tapley, B.D., Chambers, D.P., Shum, C.K., Eanes, R.J., Ries, J.C., Stewart, R.H., 1994. Accuracy assessment of the large-scale dynamic ocean topography from TOPEX/POSEIDON altimetry. Journal of Geophysical Research 99 (C12), 24605–24617.

Teague, W.J., Carron, M.J., Hogan, P.J., 1990. A comparison between the generalized digital environmental model and levitus climatologies. Journal of Geophysical Research 95 (C5), 7167–7183.

Weller, R.A., Davis, R.E., 1980. A vector measuring current meter. Deep-Sea Research 27A, 565–582.

Weller, R.A., Rudnick, D.L., Payne, R.E., Dean, J.P., Pennington, N.J., Trask, R.P., 1990. Measuring near-surface meteorology over the ocean from an array of

surface moorings in the subtropical convergence zone. Journal of Atmospheric and Oceanic Technology 7 (1), 85–103.

WOA-94. 1994. World Ocean Atlas 1994. US Department of Commerce, National Oceanic and Atmospheric Administration, National Environmental Satellite, Data, and Information Service, National Oceanographic Data Center, National Climate Laboratory, Washington, DC.

Woods, J.D., 1985. The physics of thermocline ventilation. In: Nihoul, J.C. (Ed.), Coupled Ocean–Atmosphere Models. Elsevier, Amsterdam, pp. 543–590.

Young-Molling, C.C., da Silva, A.M., Levitus, S., 1995. Atlas of Surface Marine Data 1994 Supplement A. Anomalies of Directly Observed Quantities and Surface Marine Fluxes for 1990–1993. NOAA Atlas NESDIS 6, US Department of Commerce, Washington, DC.